Influence of Population Variability in Ligament Material and Vertebrae Geometry on Cervical Spine Responses

Yash Niranjan Poojary, Jonas Östh, Johan Davidsson, Jobin John, Johan Iraeus

Abstract As future vehicles move toward increased automation, occupants will be able to adopt a wider range of postures, creating new challenges for the assessment of cervical spine injury risk when designing restraint systems. Human Body Models (HBMs) address these challenges by enabling injury investigation and prediction, including population variation in occupant responses by morphing or scaling. In this study, an average male finite element model of the cervical spine was developed, calibrated to incorporate ligament slack, and validated. Population variability in vertebral geometry and ligament material properties was then introduced to evaluate their effects on cervical spine response.

Range of Motion validations showed all functional spine units from C2–C3 to C6–C7 were within experimental corridors, with flexion-extension responses closest to the average experimental data. For flexion-extension motions, the segmental Instantaneous Center of Rotation were within experimental bounds. Population analysis indicated vertebral geometry contributed more to response average variability than ligament material properties. By varying both geometry and material, the simulation reproduced 22–71% of experimental variability.

Accurate population-level HBMs should therefore account for both geometric and material variability, and future cervical spine models would benefit from incorporating ligament slack due to its influence on the mechanical response.

Keywords Cervical spine, HBM, functional spine unit, Ligament slack, Population analysis.

I. INTRODUCTION

Cervical spine injuries are frequently under-reported in crash databases, making their true prevalence and injury mechanisms difficult to fully assess using only retrospective data of Motor Vehicle Crashes (MVCs) [1-2]. Nevertheless, the most common MVC cervical spine injuries are classified as Abbreviated Injury Scale (AIS) 1, such as whiplash-associated disorders that may lead to permanent impairment [3]. The most common moderate-to-severe MVC cervical injuries (AIS2+) are compression fractures and dislocations in the lower cervical spine [2][4-5]. Among front-seat occupants, drivers are at a higher risk of sustaining these injuries in frontal crashes [5], whereas rear-seat passengers face an overall greater risk of cervical injuries across all crash types [6]. Despite advancements in occupant safety, in modern vehicles, the number of cervical spine injuries has not decreased over time [7-10]. Furthermore, reclined, turned or sideways seating postures increase the likelihood of neck injuries [11-12], and with future vehicles moving toward increased automation, seating posture may become more variable, potentially increasing the risk of cervical spine injuries.

In MVCs, the cervical spine serves as a load path between the head and torso. During a crash, inertial head motions can generate relative motion between head and torso, leading to unphysiological cervical spine deformation in frontal, side and rear-end impacts [13]. Injuries may also result from direct head impacts with the vehicle interior, which can load the neck in compression through both direct impact forces and indirect inertial effects when head motion is constrained relative to the torso [14]. Several other injury mechanisms and injury types have been described in the literature, such as flexion-compression (wedge fracture, AIS2+), flexion-tension (facet dislocation, AIS2), extension-compression (compression fractures, AIS2+) and lateral bending and compression (facet dislocation, AIS2) [15]. These mechanisms involve different cervical structures, such as

Y. Niranjan Poojary (e-mail: yash.niranjanpoojary@chalmers.se; tel: +46 317 722 414) is a PhD student, J. Östh, PhD, is an Adjunct Associate Professor, J. John and J. Iraeus are Researchers and J. Davidsson is an Associate Professor at the Department of Mechanical Engineering at Chalmers University of Technology, Gothenburg, Sweden. J. Östh is also a Technical Expert at the Volvo Cars Safety Centre, Gothenburg, Sweden. All authors are associated with SAFER – Vehicle and Traffic Safety Centre at Chalmers, Gothenburg, Sweden.

ligaments (e.g. capsular ligaments associated with AIS1 injuries) and facet joints, reflecting their distinct contributions to injury initiation and propagation [15-16]. Collectively, these findings highlight the complex biomechanics of cervical spine injuries and the challenges of studying them experimentally [17].

Finite Element (FE) Human Body Models (HBMs) are computational models that provide a viable complement to physical experiments for studying and predicting cervical spine injury mechanisms. They can also be used for prospective studies of restraint system performance. These models offer a detailed representation of human anatomy, allowing prediction of tissue-level responses in omnidirectional loading. HBMs can be adapted to represent different subpopulations by morphing or scaling [18]. The anatomical details and population-specific adaptability of HBMs make them an advancement over traditional crash test dummies, enabling evaluation of detailed injury mechanisms and thus accurately predicting injuries.

Many cervical spine models for FE HBMs capable of assessing injuries have been reported in the literature [19-23] but their geometries are typically based on a single individual and may not represent the target subpopulation (for example, an average-sized male). Ligament material properties in these models are often based on isolated experimental tests [24]. These properties do not necessarily represent ligament in situ properties (for example, the initial length of the ligament corresponding to a given posture), which may prevent the model from capturing the Neutral Zone (NZ), an important mechanical property of the cervical spine [25]. While the effect of NZ may not be evident in global responses, it can influence tissue-level responses that are critical for studying cervical spine injuries.

Cervical spine FE models are validated using physiologic range of motion (RoM) tests [21][23]. However, RoM alone does not fully capture all nuances of cervical motion [26]. Including the Instantaneous Center of Rotation (ICR) in validation enables a more detailed evaluation of the joint properties and resulting segmental kinematics. Current cervical spine FE development workflows do not account for population variability. Differences in experimental subjects arising from variations in geometry and material properties can influence the results. Quantifying and modelling these individual differences can improve understanding and extend the applicability of the model. Together, RoM and ICR validation, along with population-based studies, form the first step toward building reliable cervical spine models for studying cervical spine injuries.

The aim of this study was to develop and validate a cervical spine FE model representing an average male and to quantify how population variability in vertebral geometry and ligament properties influences cervical spine responses. This work is intended as an initial step toward incorporating population variability in future cervical spine injury risk assessments with the developed model.

II. METHODS

A detailed FE lower cervical spine model, including the C3–C7 vertebrae, aimed at impact biomechanics injury prediction in a full HBM was developed, according to the workflow outlined in Fig. 1. In summary, the geometry was based on an individual and adjusted using literature sources to aggregate average male geometric data with focus on vertebrae body and facet joint anatomy. Material models for the hard tissues (cortical and trabecular bone) were taken directly from literature sources, whereas soft tissue material models (ligaments, intervertebral disc (IVD), and facet cartilage) were calibrated using data from recent biomechanical studies. Further, the unstretched lengths of ligaments in intact Functional Spine Units (FSUs) were calibrated based on a recent cervical spine stepwise-reduction study. The developed model was validated against published kinetic and kinematic data, and a population variability study was conducted to assess the influence of vertebral geometry and ligament material variability on the response.

The FE model was developed for the LS-DYNA (ANSYS/LST, Livermore, CA) explicit FE solver. All simulations were performed using LS-DYNA MPP_S R12.2.2 on 8 CPUs. Model pre-processing was done using ANSA v23.1.2 (Beta CAE Systems, Luzern, Switzerland), MATLAB R2023b (Mathworks Inc., Natick, MA, USA), and post-processing using LS-PREPOST v4.10 (ANSYS/LST, Livermore, CA) and Jupyter notebooks using the Dynasaur Python library [27].

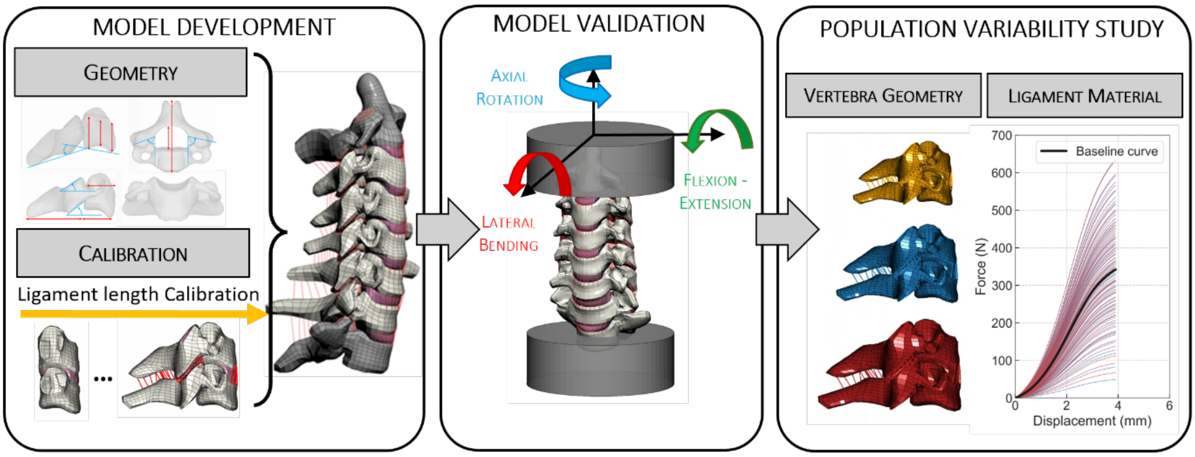

Fig. 1. Workflow of cervical spine FE model development, calibration, validation, and population variability study.

Cervical Spine FE Model Geometry

A cervical spine FE mesh was generated based on a 50th percentile female subject [28] using a meshing procedure described in [29]. The model was built using a hexahedral block design with connected nodes between vertebral bodies and discs (Fig. 2(c)). Trabecular bone and facet cartilage were modelled with hexahedral elements, cortical bone and endplates with shell elements, and ligaments as beam elements. The IVDs were modelled using a combination of solid elements for the nucleus and annulus ground, and membrane elements for annulus fibers (Fig. 2(c) and modelling details in Table I). The 50th percentile female cervical spine model was morphed into an average male in two steps. First, the model was scaled to an overall length of 125 mm, and the vertebral positions were adjusted to match an average male in an automotive seated posture based on [30-31]. Second, individual vertebrae were morphed to match an average male using global and local parameters (Fig. 2(a)–(b)).

Global parameter (Fig. 2(b)) targets for morphing were defined based on the selected literature sources (Table AI, details of the search and screening process are provided in Appendix A). The parameters included the height, width, and depth of the vertebral bodies, and the heights of the IVDs (Fig. 2(b) and parameter descriptions are provided in Table AII).

Local parameter targets (Fig. 2(b)) for morphing were defined based on literature sources and are summarised in Table AIV. Facet joint size and orientation were defined according to [32-33], and the facets were covered with a cartilage layer with thickness a between 1 mm and 1.4 mm [34]. The vertebral body cortical bone and endplate were assigned thicknesses ranging from 0.41 mm to 1.3 mm based on medical imaging studies [35-36]. The IVDs were modelled to include the nucleus pulposus, annulus fibers, and annulus ground substance. The annulus fibers were represented using three layers of membrane elements (limited by mesh discretisation), with each layer assigned a uniform fiber orientation ranging from 46° to 61° between layers (beta angles in Table I) [37]. The membrane elements had a thickness of 0.07–0.27 mm [38-39]. The nucleus pulposus occupied 30–47% of the total disc cross-sectional area [40]. Ligament cross-sectional areas were taken from [41], and ligament insertion points were defined according to [38]. A detailed description of all parameters is provided in Table AV.

Final morphing targets were obtained by proportionally adjusting the central heights of individual vertebrae and IVDs to match overall spinal length and curvature (global parameters), and by assigning discrete targets for local parameters (facet orientation and size). The cervical spine FE model was then morphed to these targets using a combination of the direct morphing tool in ANSA and radial basis function interpolation with thin-plate splines in MATLAB.

Contacts in the cervical spine FE model were defined using *AUTOMATIC_SINGLE_SURFACE for all shell elements, with a friction coefficient of 0.1 except for the facets, which used 0.01. Facet surfaces were also modelled with *AUTOMATIC_GENERAL to handle edge-to-edge interactions.

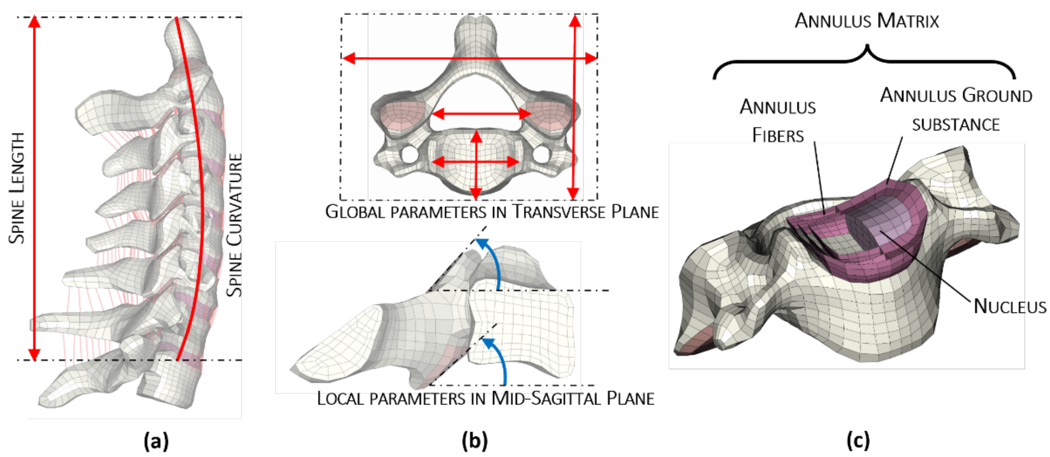

Fig. 2. (a) FE representation of the lower cervical spine (C2–T1), showing the global geometry parameters overall spinal curvature and overall length. (b) Schematic representation of selected global (red) and local (blue) geometric parameters for the C4 vertebra. (c) Isometric view of the C4 vertebra and its adjacent IVD, highlighting the components of the FE disc.

Cervical Spine FE Model Material Properties

The vertebrae were divided into anterior and posterior regions, each further subdivided into cortical and trabecular bone. Homogeneous material properties were assigned to the cortical and trabecular bone within each region, assuming uniform mechanical properties within each bone. The anterior region of the vertebral body was modelled using an anisotropic material formulation, with the primary stiffness oriented in the inferior–superior direction. The cortical bone was defined as transversely isotropic, and the trabecular bone was modelled as an orthotropic material [42]. The posterior region of the vertebra was defined as isotropic, as described in [42].

The annulus fibers primarily determine disc tension, and their material properties, estimated from experimental data [43], define the tensile response in the IVD. Accordingly, the nucleus pulposus and annulus ground substance are not included in carrying tensile loads, and their compressive behaviour was modelled using an Ogden rubber formulation with parameters calibrated from confined compression tests [44]. Facet cartilage was modelled with a separate Ogden formulation calibrated from confined compression test data [45] (modelling details are provided in Appendix B and material parameters are listed in Table I).

The Anterior Longitudinal Ligament (ALL), Posterior Longitudinal Ligament (PLL), Ligamentum Flavum (LF), Capsular Ligament (CL) and Interspinous Ligament (ISL) were modelled using nonlinear elastic beam elements with force-deflection and strain rate properties based on [24]. A summary of the material implementations using LS-DYNA constitutive models is shown in Table I.

TABLE I

SUMMARY OF LS-DYNA MATERIAL AND ELEMENT PARAMETERS (UNITS IN mm, ms and GPa)

Part	ELFORM (IHQ)	Material Model (*LS-DYNA material number*)	Model Parameters	References
Vertebra body				
Anterior Cortical bone		Transversely isotropic *(*MAT_157)*	C_{11}=19.9, C_{12}=7.5, C_{13}=7.5, C2$_2$=17.0, C23=7.75, C_{33}=17.0, C_{44}=3.5, C_{55}=4.0, C_{66}=3.5, S_{11}=0.112, S_{22}=0.053, S_{33}=0.053, S_{12}=0.047	[42]
Posterior Cortical bone	Quadrilateral shell type 10 (Stiffness based 5)	Isotropic elastic–plastic *(*MAT_024)*	E=16.4, ν=0.235, σ_Y=0.112, E_{tan}=0.924	[42]
Anterior trabecular bone		Orthotropic elastic *(*MAT_2O)*		[42][46-47]
Posterior trabecular bone		Isotropic elastic–plastic *(*MAT_024)*	E=0.492, ν=0.1	[42]
Endplate		Isotropic elastic–plastic *(*MAT_024)*	E=0.193, ν=0.3, σ_Y=0.0037	[42]
Intervertebral disc				
Annulus fibers	Quadrilateral Membrane	Orthotropic nonlinear elastic *(*MAT_034)*	**(IN)** E_A=0.0038, E_B=0.0038, ν_{BA}=0.3, G_{AB}=0.0015, Beta= ±46°	[37][43]

	type 14		(**MID**) E_A=0.0054, E_B=0.0054, ν_{BA}=0.3, G_{AB}=0.0021, Beta= ±57° (**OUT**) E_A=0.007, E_B=0.007, ν_{BA}=0.3, G_{AB}=0.0027, Beta= ±61°	
Annulus ground substance	Hexahedral type 1 (Stiffness based 3)	Ogden rubber *(*MAT_77_O)*	ν=0.4998, μ_1=0.0025, μ_2=-0.00059, μ_3=-0.0022, α_1=-2.03, α_1=-0.468, α_1=-2.241	[44]
Nucleus Pulposus	Hexahedral type 1 (Stiffness based 3)	Ogden rubber *(*MAT_77_O)*	ν=0.49998, μ_1=0.166, μ_2=-1.029, μ_3=2.612, α_1=1.371, α_1=0.632, α_1=0.162	[44]
Facet cartilage	Hexahedral type 1 (Stiffness based 6)	Ogden rubber *(*MAT_77_O)*	ν=0.499, μ_1=0.00014, μ_2=8.904E^{-8}, α_1=17.926, α_1=0.0103	[45]
Ligaments	Beams type 6	Nonlinear elastic with rate dependency (**MAT_074)*		[24]

ELFORM = element formation in LS-DYNA; IHQ = hourglass control type in LS-DYNA.

Calibration of Unstretched Ligament Lengths

The ligament material properties were defined based on published in vitro tests [24] and therefore may not fully represent in situ ligament behaviour. One factor contributing to this difference is the initial state of the ligaments, particularly their initial (unstretched) lengths. This has been previously recognised in other parts of the spine, and compensation for unstretched ligament length has been addressed using numerical optimisation [48] or stepwise-reduction tests [42].

Stepwise-reduction test data from C2–C3, C4–C4 and C6–C7 FSUs from six post-mortem human subjects (PMHS) (3 males and 3 females, average age = 48 years) [49] were used for the unstretched ligament length calibration. The tests were performed under quasistatic moment loading and the maximum load applied was 1 Nm. For each FSU, the physical testing was carried out in seven steps (red arrow in Fig. 3), with the RoM in flexion-extension, lateral bending and axial rotation recorded at each step.

Calibration simulations were performed in opposite order (as shown by the green arrow in Fig. 3) to the physical tests to isolate and calibrate the unstretched lengths of each ligament. First, a model without ligaments and posterior elements was simulated (Step 1, Fig. 3). Then, a ligament or an anatomical structure (e.g. the posterior parts) was added one at a time. At each step, the unstretched length of the added ligament was calibrated to match the RoM from physical tests. The calibration was done by offsetting the ligament material curve along the displacement axis, thereby introducing slack and increasing the ligament unstretched length.

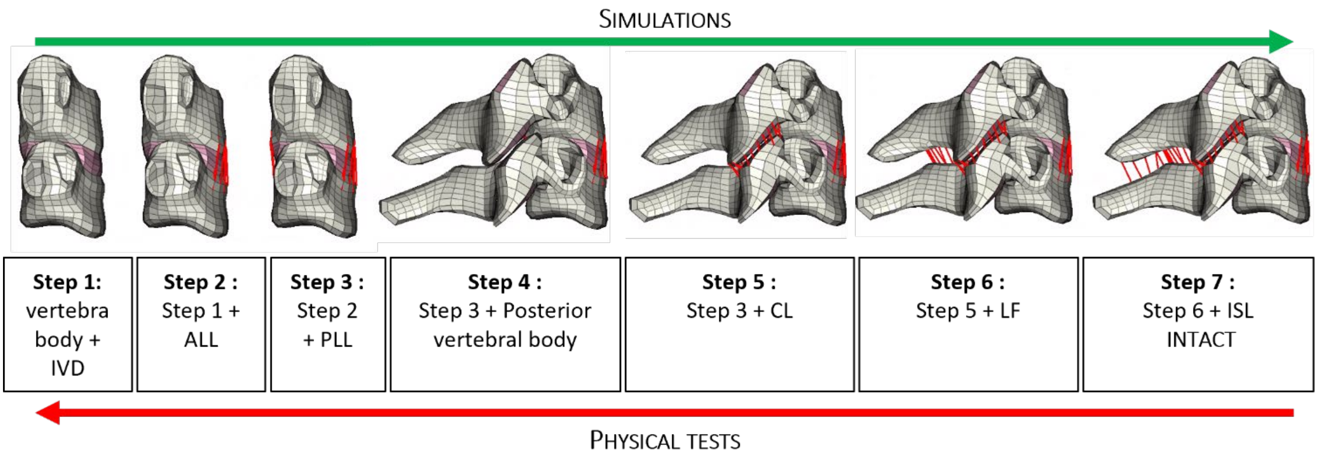

Fig. 3. Illustration of unstretched ligament length calibration in simulations (green arrow), starting with the IVD only and sequentially adding structures. Physical tests were performed in the opposite order (red arrow) [49]. IVD = Intervertebral Disc; ALL = Anterior Longitudinal Ligament; PLL = Posterior Longitudinal Ligament; CL = Capsular Ligament; LF = Ligamentum Flavum; ISL = Interspinous Ligament.

Model Kinetic and Kinematic Validation

Model validation was performed by comparing simulated and experimental RoM and ICR responses. The original tests used for validation are listed in Table II, and these datasets were not used for model calibration. The RoM validations were done at the FSU level comparing to [50-52] as well as for the full ligamentous lower cervical spine (LCS, C2–T1) comparing to [53].

In the original tests (Table II), the cranial and caudal vertebrae were potted in polyester resin (Fig. 4 and Fig. 5). This was reproduced in simulations using a penalty-based *CONSTRAINED_SHELL_IN_SOLID_PENALTY of the cortical shells in the vertebrae to the potting. The potting was modelled using solid elements and a linear elastic material with a Young's modulus of 0.92 GPa. The lower edge of the caudal potting was constrained in all Degrees of Freedom (DOFs) using a rigid body constraint, while the cranial potting was subjected to pure flexion, extension, and lateral bending. In the original tests, pure moments were applied incrementally until the maximum moment was reached. In the simulations this loading was replicated using a smooth displacement controlled *BOUNDARY_PRESCRIBED_MOTION at 0.050 deg/ms with a ramp-up time of 100 ms, considered representative of quasistatic speeds.

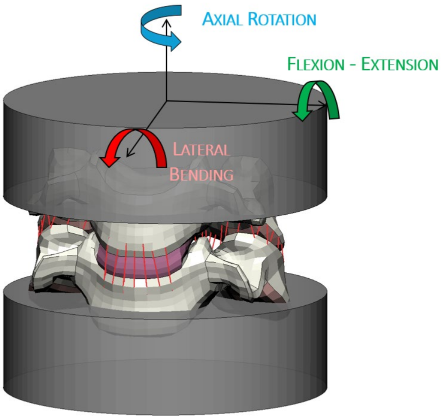

Fig. 4. Validation set-up for C4–C5 FSU tests [49-52]. The potting is shown in grey. The cranial (top) potting was subjected to pure moments, and the caudal (bottom) potting was fixed in all DOFs. The arrows show the loads in the simulation.

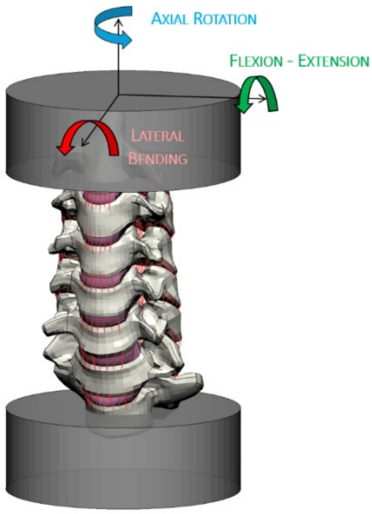

Fig. 5. Validation set-up for full LCS tests [53].

The ICRs in the sagittal plane were evaluated in pure flexion-extension under quasistatic loading and the maximum load of 1.5 Nm. The simulation was performed using the same test set-up and boundary conditions as in the RoM tests (Fig. 4). ICRs were calculated at 0.2 degree rotation increments, starting at 100 ms (the ramp-up time), resulting in 20 instances across the motion. The simulated ICRs were determined at each increment from the nodal displacement vectors of two reference nodes located anterior and posterior on the cranial vertebra's superior endplate in the mid-sagittal plane, following the method described in [54-55]. The simulation ICRs were compared with a representative envelope (constructed using kernel density estimation) derived from the physical test data [26].

TABLE II
DETAILS OF THE DATA SOURCES USED FOR VALIDATION

Source	Validation type	Specimen Information		Test information	
		Age (years)	Specimens (% males)	Loading type	Loading speed (maximum load)
Panjabi *et al.*, 2001 [50]	RoM	-	16 LCS (-) *	FE, LB, AR	Quasistatic (1 Nm)
Wheeldon *et al.*, 2006 [51]	RoM	33.4 ± 11.7	13 LCS (72) *	FE	Quasistatic (2 Nm)
Nightingale *et al.*, 2007 [52]	RoM	66 ± 7.2	26 FSU (100)	FE	Quasistatic (3.5 Nm)
Barrey *et al.*, 2015 [53]	RoM	62 ± 6.4	12 LCS (50)	FE, LB, AR	Quasistatic (2 Nm)
Jonas *et al.*, 2018 [26]	ICR	47.5	18 FSU (50)	FE	Quasistatic (1.5 Nm)

LCS = ligamentous cervical spine (C2–T1); FSU = Functional spine unit – two vertebra and adjacent disc; FE = Flexion-extension; LB = Lateral bending; AR = Axial rotation.

** Simulation done with an FSU comparing the segmental responses due to unknown LCS initial posture.*

Vertebra Geometry and Ligament Material Population Variability Study

A parametric analysis was carried out to study the influence of geometry and ligament material variability on the flexion-extension response of the C4–C5 FSU, and the results were compared with test data reported in [52]. Variability in both vertebral geometry and ligament material was modelled using Gaussian distributions, with parameters derived from experimental data.

Geometric variability was captured using a single parameter, which defines combined variability along the three global axes. Full correlation among vertebral body dimensions was applied, as indicated by [56]. The vertebral body scale is defined in three axes ($\boldsymbol{x}$: anterior-posterior, $\boldsymbol{y}$: medial-lateral and $\boldsymbol{z}$: inferior-superior). The single variation parameter was multiplied by the standard deviation (SD) of each axis (σ_x= 1.64 mm, σ_y= 1.63 mm and σ_z= 1.32 mm), calculated from the pooled data used to derive the geometry, to determine the scaling factor. To prevent non-physiological geometries, the variation parameter was sampled from a truncated normal distribution with bounds of ±2 SD. This approach preserved the relative proportions of the vertebra while allowing variation in overall size. The resulting global scaling factor was implemented using *DEFINE_TRANSFORMATION in LS-DYNA.

Ligament material variability was based on experimental data [24], which was used to define the baseline material properties. Variability was implemented as a scale factor in LS-DYNA, scaling the force axis (ordinate) in the force-deformation characteristics of each ligament. Similar to the geometry parameter, ligament scaling factors were sampled from truncated normal distribution with bounds of ±2 SD. To address uncertainty in correlations among ligaments within a FSU, two hypotheses were considered. According to the first hypothesis, all ligaments within an FSU were strongly (perfectly) and positively correlated, whereas according to the second hypothesis, ligament properties are fully independent of each other. Based on these hypotheses, two groups of samples were generated for the parametric study.

For the first group, two parameters were sampled, one geometric and one ligament parameter, while for the second group, six parameters were sampled (one geometric and five ligament parameters). For each group, 50 Latin Hypercube Samples (LHS) were generated based on the parameter distributions presented. Each group's ability to capture experimental variability was assessed by comparing the ±1 SD of the test RoM with the ±1 SD of the simulated RoM at moments ranging from 0.5 Nm to 3.5 Nm.

III. RESULTS

The cervical spine model was morphed to vertebral geometries representative of an average male in an automotive seated posture. Morphing was guided by global targets from Table AIII and local targets from Table AV. For example, the C4–C5 FSU in the mid-sagittal view (Fig. 6(a)) and the C4 vertebra in the superior (transverse) view (Fig. 6(b)) show that the post-morphed vertebrae are consistent with the global targets (blue dots). Disc dimensions, such as centre height, result from vertebral height adjustments under posture constraints and remain within experimental measurement ranges (disk centre height in Table AII). The resulting local parameters, including facet orientation and size, are within the reported ranges (Table AV). Differences between the morphed model and target values arise from preserving mesh quality. The developed model contains approximately 28,000 hexahedral solid elements, 18,000 quadrilateral shell elements, and 574 beam elements. All elements met the quality criteria of Jacobians greater than 0.3 (92% of elements > 0.7) and aspect ratios below 10 (90% of elements < 3).

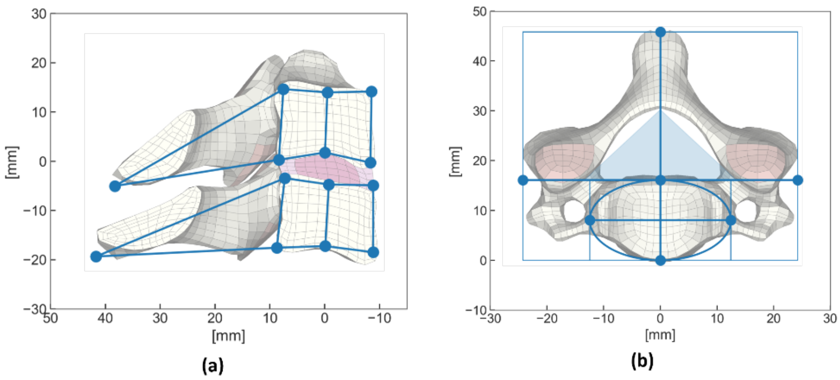

Fig. 6. (a) Mid-sagittal geometry of C4–C5 (background) morphed to the target geometry (blue). (b) Superior view (from the transverse plane) of the C4 vertebra (background) morphed to the target geometry (blue).

Material and Ligament Unstretched Length Calibration

Calibration of the ligament unstretched lengths for the C4–C5 segment resulted in added slack of 0 mm for the ALL, 1 mm for the PLL, 2 mm for the CL, 1 mm for the LF and 0 mm for the ISL. The resulting baseline model RoM was within the limits of the physical test results across all steps of flexion-extension (Fig. 7(a)) and axial rotation (Fig. 7(b)). In lateral bending, the baseline model already had a higher stiffness for step 1 (IVD only) than the physical tests (Fig. 7(c)). The axial rotation of the baseline model shifts from a higher RoM (compliant model) at step 3 to a lower RoM (stiff model) at step 4 following the addition of the posterior components. Similar patterns for calibration results were seen for other FSUs and are shown in Appendix C. However, calibration of unstretched lengths in C2–C3 and C6–C7 resulted in different slack values compared to C4–C5 and are reported in Table CI. The model incorporating the geometry updates and ligament slack is hereafter referred to as the baseline model.

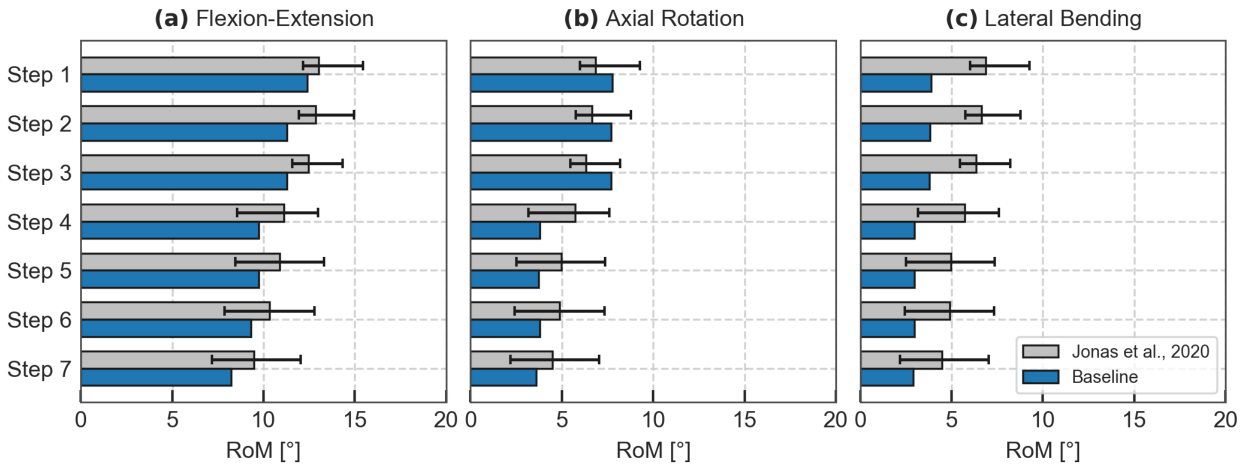

Fig. 7. Resulting C4–C5 FSU RoM for post-calibration, compared to Jonas *et al*. [49].

Model Kinetic and Kinematic Validation

Results from the C4–C5 FSU validations are shown in Fig. 8 and the other FSU levels are presented in Appendix D. In flexion-extension, the baseline model response was close to the average of the experimental data [50-52] and within the experimental corridor. In axial rotation, the model response fell within the experimental response corridor [50], except for very low moments around the neutral zone. In lateral bending, the model was stiffer at low moments, indicating that part of the neutral zone observed in the physical experiments [50] was not captured. However, with increasing moment the model lateral bending moment approached the experimental corridor. Please note that the physical test corridor is asymmetric. A similar pattern was observed for the other FSUs, Appendix D except for C6–C7, for which the model response in axial rotation fell outside the experimental corridor on the lower stiffness side, while the lateral bending response remained within the experimental corridor.

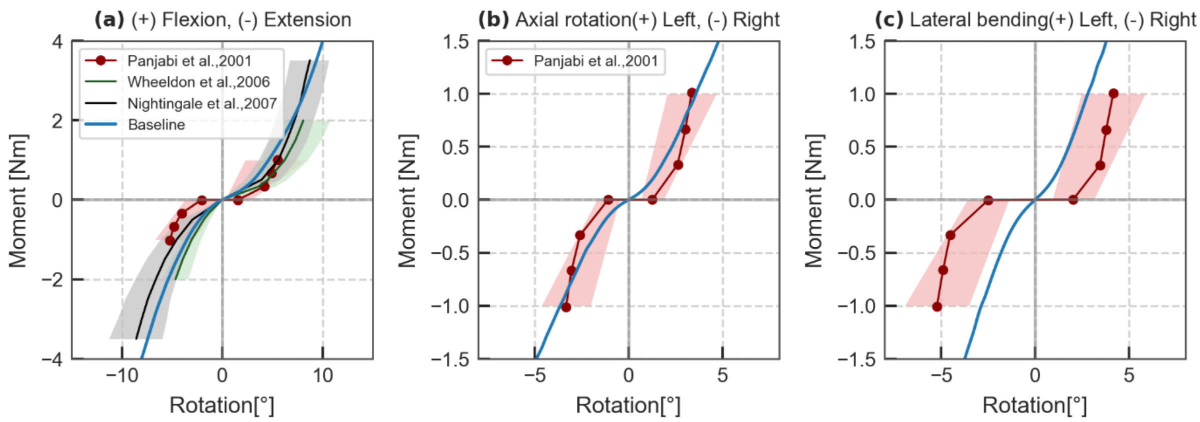

Fig. 8. Resulting validation of C4–C5 FSU moment-rotation response, compared to [50-52]. *Note:* the axes limits used for flexion-extension are different from the other two plots.

In the validation (Fig. 9) of the C2–T1, the baseline model had a stiffer response than the experimental test data in flexion, while in extension the model response fell within the physical test range [53] for applied moments below 1 Nm, but underpredicted stiffness at higher moments (Fig. 9(a)). In axial rotation, the baseline model response was within experimental range at low applied moments but underpredicted the stiffness at moments above 1 Nm (Fig. 9(b)). In lateral bending, the baseline model matched the rotation at 1.5 Nm of the experimental test data but was outside the test response range at lower moments on the stiffer side (Fig. 9(c)).

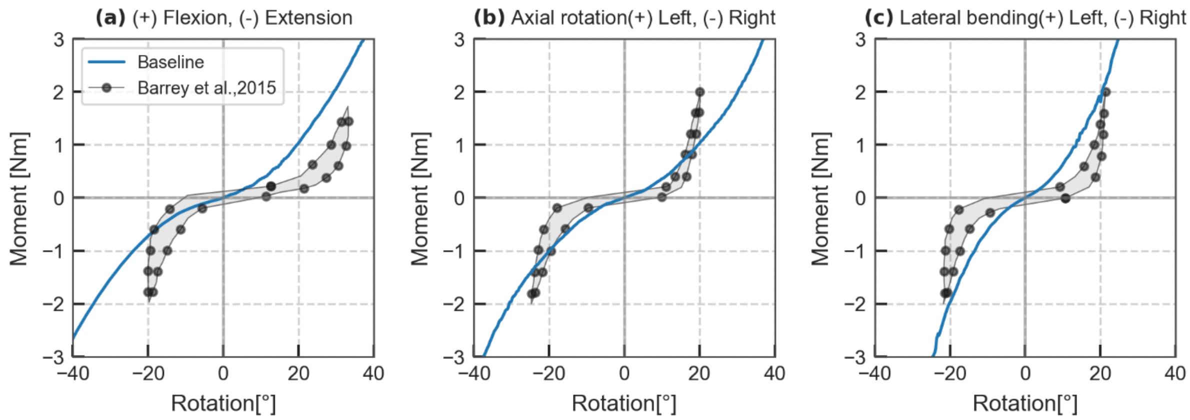

Fig. 9. Resulting validation of the C2–T1 baseline model moment-rotation response, compared to Barrey *et al*. [53].

The simulated ICRs in flexion-extension remained within the representative envelope [26] (Fig. 10). During flexion, the ICRs shifted to a more superior position compared to extension. The extension ICRs were outside (in the limit) of the 50% envelope (black envelope in Fig. 10). The simulation ICRs remained almost constant, in contrast to the wider spread observed in the physical tests. Similar patterns are seen for the other FSU (Appendix D).

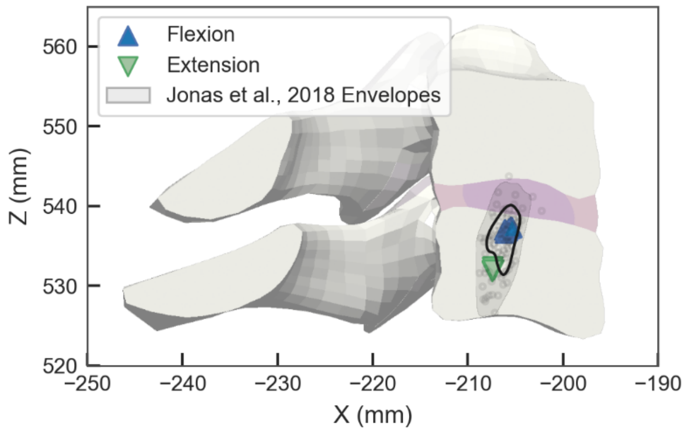

Fig. 10. Resulting segmental ICRs for C4–C5, blue markers (10 markers) representing ICRs in flexion (10 markers), green in extension. The black envelope shows the 50% highest density region (HDR), representing the most probable region of ICRs in physical test data (combined for flexion and extension), while the shaded grey envelope shows the 95% HDR, showing most of the observed variability in Jonas *et al*. [26].

Vertebra Geometry and Ligament Material Population Variability Study

A total of 204 simulations (one baseline and 50 sampled model variations each for flexion and extension within each parameter group) were conducted, and all simulations completed successfully without error terminations. The C4–C5 flexion-extension responses for both the two-parameter and six-parameter groups are presented in (Fig. 11(a)). The model with variations from both parameter groups visually captured the spread observed in the test data. However, comparing the ±1 SD ratio between the simulated and experimental responses (Fig. 11(b)) showed that both parameter groups underestimated the variability in both extension and flexion. For flexion, the model captured more variability than for extension, and more variability was captured at higher applied moments (up to 3.5 Nm). At lower moments, both parameter groups performed similarly, whereas at higher moments the two-parameter group captured a greater portion of the experimental variability in flexion.

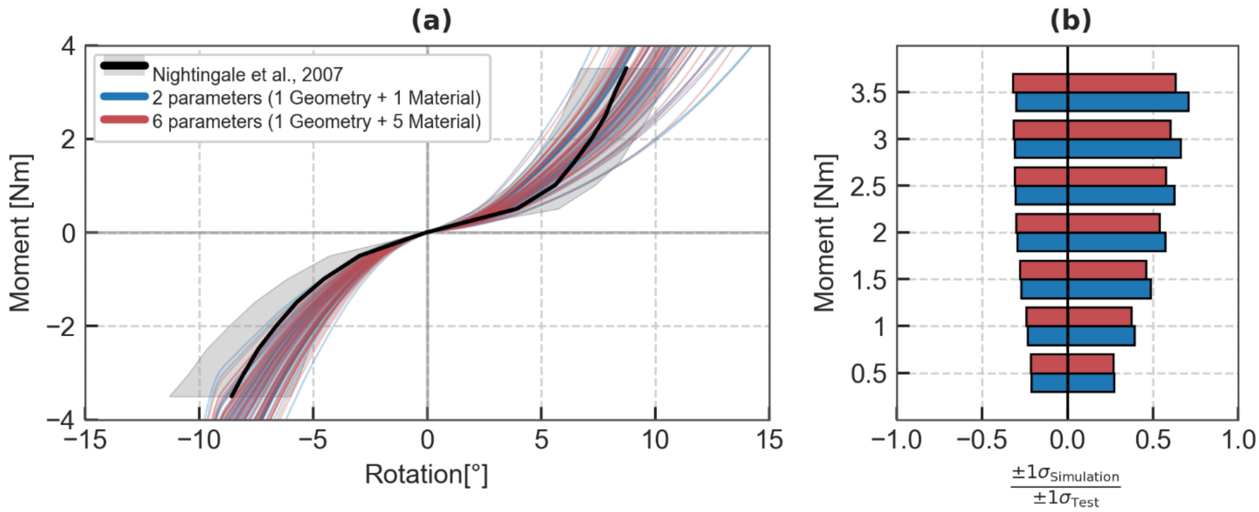

Fig. 11. (a) Flexion (positive) and extension (negative) response for C4–C5 compared to the average and ±1 SD corridor reported in [52]. (b) Ratio of the ±1 SD of RoM predicted by the simulations to the ±1 SD measured in the experiments at different moments. A |ratio| = 1 represents the simulation perfectly captures the variability, |ratio| < 1 represents underestimation of variability by the simulation. Positive values represent flexion and negative extension.

IV. DISCUSSION

In this study, a detailed FE model of the average male lower cervical spine was developed using geometries derived from literature data. The unstretched ligament lengths (Table CI) were calibrated using results from a recent stepwise-reduction physical test [49], which were not available during the development of previous cervical spine FE models. Model validation was performed using RoM and ICRs, which complemented each other in capturing the model's mechanical stiffness and spinal kinematics. Following calibration and validation, the model was used to study the influence of population variability of vertebral geometry and ligament material on the mechanical response of the cervical spine.

The developed model represents the average male lower cervical spine, with vertebral geometries derived from multiple literature sources to capture both overall geometry (global parameters) and detailed anatomical geometry (local parameters). The resulting target geometry (global in Table AIII, local in Table AV) can also be used as a reference for future modelling, including morphing models to average male size. The data were obtained from studies using different measurement techniques, including physical measurements, CT scans, and X-rays. Population characteristics, including age, height, and weight, were used to select and combine literature data, defining a representative "average male" vertebra (Table AI). Existing FE models often rely on subject-specific geometries that are average in a global sense (e.g. average stature), whereas the developed model is also average in local measurements and thus closer to a "true" population average male.

The developed model used rate-dependent ligament materials based on published in vitro tests [24]. These data do not fully represent in situ ligament behaviour, requiring the calibration of unstretched ligament lengths [42][48] to establish a compensating slack. In the current study, FE model slack was calibrated using stepwise-reduction tests. In the first step of the calibration (without ligaments and posterior parts), the predicted responses for all loading modes fell within experimental ranges except for lateral bending (see detailed data in Appendix C). This indicates that the IVD contribution to lateral bending is too high in the model. Adjusting IVD material parameters to improve lateral bending responses could compromise overall model stability.

In the FE model, nucleus and annulus areas were matched to the literature, but the detailed disc anatomy was not modelled. Anatomy studies describe the cervical disc as having a thick, crescent-shaped anterior annulus with obliquely oriented fibers, and a thin posterior annulus with primarily vertical fiber orientation [38][57]. Furthermore, the material properties of the annulus ground and the nucleus were primarily derived from compression tests [44], leaving their tensile behaviour uncontrolled. A complete characterisation of disc mechanics would require physical tests of isolated discs in compression-tension and quantifying load sharing between the nucleus and annulus. However, to the best of the authors' knowledge, such data are not available in the literature.

Validations of the FSUs and the full LCS were conducted in flexion-extension, axial rotation, and lateral bending. The predicted segmental responses in the RoM tests were within the experimental corridors (Fig. 8 and Appendix D), indicating that the model reproduces biofidelic segmental responses over the validation range (quasistatic loading up to 3.5 Nm). In the full LCS validation (Fig. 9), the model predicted a stiffer flexion response than the experimental data, while it underpredicted the stiffness in extension for moments exceeding 1 Nm. The experimental set-up specified the orientation of the caudal vertebra (T1 in the current validations) during potting but did not provide any details on spinal curvature. The baseline model used a curvature representative of an automotive seated occupant, which may not match the curvature of the specimens used in the physical tests. Comparing the simulation and experimental flexion-extension results, the physical specimens may have been positioned relative to the baseline model in a pre-extended state. This configuration could have led to earlier engagement of the facet joints, resulting in a stiffer response in extension and, consequently, also influencing flexion behaviour.

Further, the baseline model was validated for local kinematics using segmental ICRs in flexion-extension. In the simulations, flexion and extension ICRs differed consistently across all three evaluated FSUs (Fig. 10 and Appendix D), with flexion ICRs located more superiorly than extension ICRs. Comparison with experimental data was limited, as separate ICRs could not be determined due to manual digitisation. In the simulations, the superior position of flexion ICRs aligns with the roles of discs and ligaments, resulting in a smaller bending radius. At the same time, extension, primarily guided by the facet joints, allows increased translational motion, resulting in more inferior ICRs matching the descriptions in [49]. It is hypothesised that the experimental measurements include variability, due to measurement noise, limitations of the reference coordinate system, and other methodological uncertainties [26], whereas the predicted ICR from simulation does not, which is one reason for the larger spread in the physical data. Experimental results suggested that more caudal cervical motion segments have ICRs located closer to the inferior endplate, with their position becoming more consistent (less variable) in lower segments [49], a pattern also reported in previous studies [54]. This trend was also observed in the simulations performed in the present study.

Population variability in vertebral geometry was implemented using pooled standard deviations from the literature sources used to build the baseline model. In addition, full correlation was assumed among vertebral geometric measures in the population variability study, as the correlations between measures are unknown. Comprehensive specimen-level datasets reporting all relevant geometric measurements for individual vertebrae would help address this limitation, but, to the authors' knowledge, such data are currently unavailable. Ligament material variability was represented using two hypotheses based on correlations between ligaments within an FSU. The Pearson correlations between ligament linear stiffnesses within an FSU (Appendix E) were generally weak, indicating that ligament stiffnesses do not change consistently or proportionally within an FSU. However, the correlation trends were inconsistent across loading speeds and based on a single subpopulation (conclusion based on one dataset) [24], so in order to explore the potential impact of ligament variability, population analyses were performed for both hypotheses (referred to as groups in the simulations).

Applying variations to geometry and ligament material properties in simulations of FSU flexion-extension tests allowed the model to capture a major part of the spread observed in experimental tests (Fig. 11(a)), with both groups capturing experimental variability to the same extent. Figure E4 illustrates the most compliant and stiffest models from the two-parameter group, for which the smallest FSU corresponded to the most compliant model and the largest FSU to the stiffest. In the six-parameter group, the model stiffest in flexion was not the stiffest in extension (Fig. E5, % variation in Table EII), indicating that variations in ligament material properties influence the model's behaviour. Overall, independent ligament variations had a limited impact on the total variability captured, as geometric variations dominated. Moreover, the geometry scaling in the current model affects the IVD size (changes the disc height and cross-sectional area), influencing its mechanical response and suggesting that the resulting variations are not purely geometric. The current implementation does not fully explore the effects of the independent ligament hypothesis, and future studies should examine whether ligament-specific variability should be included in population-level analyses and safety evaluations.

The population variability results further show that the model captures more of the experimental variability in flexion than in extension (27–71% in flexion and 21–32% in extension). In flexion, motion is largely controlled by ligament stretching (as observed in the ICR validation), and changes in geometry affect ligament leverage relative to the rotation centre, explaining the observed variability. In extension, FSU response is more influenced by the local geometry, such as facet orientations [58] (also reflected in the ICR validation). This was not fully represented by the geometric variations implemented in this study, limiting the model's ability to capture the experimental variability.

The population study and validations showed that geometric variability and the initial curvature of the spine affected RoM responses, showing the importance of accurately representing them in the model. A limitation in the unstretched ligament length calibration in this study was the unavailability of these data, i.e. individual specimen geometry and the starting positions at each calibration step. Thus, assumptions were required: (1) that the test was performed using samples representative of the baseline model (average male); and (2) that all calibration steps were assumed to start from the same position. However, the second assumption may not be true, as removing a ligament can alter the FSU's neutral posture. Also, ligaments farther from the centre of rotation are expected to exhibit greater slack, but this was not observed in the current calibration results (ligament slacks did not show such a trend). In addition to the already mentioned uncertainty around starting position, the lack of trend may also be due to differences in the toe-region lengths of ligament force-deflection curves, which are influenced by the tested ligament length. Future studies would benefit from more detailed descriptions of spinal curvature along with specimen geometric data in stepwise-reduction tests. Including ligament in situ length information in ligament material testing would further improve model accuracy and reduce uncertainty in model predictions.

Studies have shown the importance of modelling localised geometry, such as the facets, can influence both global [59] and tissue-level responses [58] of the cervical spine. The current population study assumes that all vertebral dimensions are fully correlated, which is not necessarily true. Statistical Shape Models (SSMs) provide a better way to describe the variations in vertebral geometry while preserving local geometry covariation. Existing cervical spine SSMs primarily capture overall spine geometry and posture [31], rely on a limited number of landmarks to represent the geometry [60], or are derived for only part of the cervical spine [61]. A complete cervical spine SSM, complemented with detailed three-dimensional vertebral measurements, would be an important step forward.

This study calibrates ligament slack and quantifies population variability under quasi-static loading; validation is therefore limited to physiological, non-injurious conditions. Extending the model to injury prediction and evaluation requires validation under dynamic loading and at injurious thresholds at the FSU and ligamentous cervical spine levels, complemented by full-body validation after HBM integration. Accounting for posture-dependent slack across seated, standing, and reclined alignments would further improve physiological representation in HBMs. Collectively, these steps would strengthen cervical spine injury prediction and evaluation using HBMs.

V. CONCLUSION

A detailed average male lower cervical spine FE model was developed, calibrated, and validated for omnidirectional loading. Ligament slack was introduced based on stepwise-reduction tests to account for unstretched ligament length. The model validation showed that the model predicted kinetic and kinematic responses within or at the limits of experimental ranges. A population study indicated that vertebral geometry contributes more to the variability seen in physical tests than ligament material properties. Future population-level studies should account for both vertebral geometric and ligament material variability, and future cervical spine models would benefit from incorporating ligament slack, given its influence on mechanical response.

VI. ACKNOWLEDGEMENTS

This work was carried out at SAFER, Vehicle and Traffic Safety Centre at Chalmers University of Technology, Gothenburg, Sweden, and funded by FFI-Strategic Vehicle Research and Innovation, by Vinnova, the Swedish Energy Agency, the Swedish Transport Administration and the Swedish vehicle industry. The simulations were enabled by resources provided by the National Academic Infrastructure for Supercomputing in Sweden (NAISS), partially funded by the Swedish Research Council through grant agreement no. 2022-06725.

AI Disclosure: generative artificial intelligence tool (Grammarly, 2026) was used to support language editing. All scientific content, interpretations, and conclusions were developed, reviewed and validated by the authors, who take full responsibility for the accuracy and integrity of the work.

VII. REFERENCES

[1] Freeman, M. D. and Leith, W. M. (2020) Estimating the number of traffic crash-related cervical spine injuries in the United States; An analysis and comparison of national crash and hospital data. *Accident Analysis & Prevention*, **142**: p. 105571.

[2] Dutschke, J., Hutchinson, T., Jones, C., Lindsay, V. L. (2023) "Car drivers with an AIS2+ spine injury: Description of a sample from South Australia". Centre for Automotive Safety Research: The University of Adelaide

[3] Loeversund, P., Nygren, A., Salen, B., Tingvall, C. (1988) Neck injuries in rear end collisions among front and rear seat occupants. *Proceedings of the IRCOBI conference*, 1988, Bergisch-Gladbach, Germany.

[4] Yoganandan, N., Haffner, M., *et al*. (1989) Epidemiology and Injury Biomechanics of Motor Vehicle Related Trauma to the Human Spine. SAE International.

[5] Pipkorn, B., Iraeus, J., Lindkvist, M., Puthan, P., Bunketorp, O. (2020) Occupant injuries in light passenger vehicles—A NASS study to enable priorities for development of injury prediction capabilities of human body models. *Accident Analysis & Prevention*, **138**: p. 105443.

[6] Mitchell, R. J., Bambach, M. R., Toson, B. (2015) Injury risk for matched front and rear seat car passengers by injury severity and crash type: An exploratory study. *Accident Analysis & Prevention*, **82**: pp. 171–179.

[7] Al-Salehi, L., Kroeker, S. G., *et al*. (2024) Cervical vertebral and spinal cord injuries in rollover occupants. *Injury Epidemiology*, **11**(1): p. 30.

[8] Wang, M. C., Pintar, F., Yoganandan, N., Maiman, D. J. (2009) The continued burden of spine fractures after motor vehicle crashes. *J Neurosurg Spine*, **10**(2): pp. 86–92.

[9] Balmaceno-Criss, M., Lou, M., *et al*. (2024) What Is the Epidemiology of Cervical and Thoracic Spine Fractures? *Clin Orthop Relat Res*, **482**(12): pp. 2222–2235.

[10] Inamasu, J. and Kato, M. (2018) Airbag deployment and cervical spine injury in restrained drivers following motor vehicle collisions. *Neuroradiology*, **60**(12): pp. 1307–1313.

[11] Schaefer, L. C., Junge, M., Voros, I., Kocaslan, K., Becker, U. (2021) Odds ratios for reclined seating positions in real-world crashes. *Accident Analysis & Prevention*, **161**: p. 106357.

[12] McMurry, T. L., Poplin, G. S., Shaw, G., Panzer, M. B. (2018) Crash safety concerns for out-of-position occupant postures: A look toward safety in highly automated vehicles. *Traffic Injury Prevention*, **19**(6): pp. 582–587.

[13] Svensson, M. Y., Boström, O., *et al*. (2000) Neck injuries in car collisions—a review covering a possible injury mechanism and the development of a new rear-impact dummy. *Accident Analysis & Prevention*, **32**(2): pp. 167–175.

[14] Foroutan, P., Quarrington, R. D., Jones, C. F. (2024) Mechanisms and risk factors associated with spinal cord injury, facet fracture, and level of dislocation, in occupants with cervical spine dislocations sustained in motor vehicle crashes. *Traffic Injury Prevention*, **25**(8): pp. 1129–1136.

[15] Li, F., Liu, N.-s., *et al*. (2019) A review of neck injury and protection in vehicle accidents. *Transportation Safety and Environment*, **1**(2): pp. 89–105.

[16] Siegmund, G. P., Winkelstein, B. A., Ivancic, P. C., Svensson, M. Y., Vasavada, A. (2009) The Anatomy and Biomechanics of Acute and Chronic Whiplash Injury. *Traffic Injury Prevention*, **10**(2): pp. 101–112.

[17] Huelke, D. F. and Nusholtz, G. S. (1986) Cervical spine biomechanics: a review of the literature. *Journal of Orthopaedic Research*, **4**(2): pp. 232–245.

[18] Larsson, K. J., Osth, J., Iraeus, J., Pipkorn, B. (2024) A First Step Toward a Family of Morphed Human Body Models Enabling Prediction of Population Injury Outcomes. *Journal of Biomechanical Engineering*, **146**(3).

[19] Halldin, P. H., Brolin, K., *et al*. (2000) Investigation of conditions that affect neck compression-flexion injuries using numerical techniques. *Stapp Car Crash Journal*, **44**(3): pp. 127–138.

[20] Kitagawa, Y., Yasuki, T., Hasegawa, J. (2006) A Study of Cervical Spine Kinematics and Joint Capsule Strain in Rear Impacts using a Human FE Model. The Stapp Association.

[21] Panzer, M. B., Fice, J. B., Cronin, D. S. (2011) Cervical spine response in frontal crash. *Medical Engineering & Physics*, **33**(9): pp. 1147–1159.

[22] Meyer, F., Humm, J., *et al*. (2021) Development of a detailed human neck finite element model and injury risk curves under lateral impact. *Journal of the Mechanical Behavior of Biomedical Materials*, **116**: p. 104318.

[23] Östh, J., Brolin, K., Svensson, M. Y., Linder, A. (2016) A Female Ligamentous Cervical Spine Finite Element Model Validated for Physiological Loads. *Journal of Biomechanical Engineering*, **138**(6).

[24] Mattucci, S. F., Moulton, J. A., Chandrashekar, N., Cronin, D. S. (2012) Strain rate dependent properties of younger human cervical spine ligaments. *Journal of the Mechanical Behavior of Biomedical Materials*, **10**: pp. 216–226.

[25] Panjabi, M. M. (1992) The stabilizing system of the spine. Part II. Neutral zone and instability hypothesis. *Clinical Spine Surgery*, **5**(4): pp. 390–397.

[26] Jonas, R., Demmelmaier, R., Hacker, S. P., Wilke, H. J. (2018) Comparison of three-dimensional helical axes of the cervical spine between in vitro and in vivo testing. *The Spine Journal*, **18**(3): pp. 515–524.

[27] Schachner, M., Micorek, J. T., Luttenberger, P., Greimel, R., Klug, C., Rajinovic, S. (2022) Dynasaur-dynamic simulation analysis of numerical results. Internet https://gitlab.com/VSI-TUGraz/Dynasaur.

[28] Gayzik, F. S., Moreno, D. P., *et al*. (2011) Development of a Full Body CAD Dataset for Computational Modeling: A Multi-modality Approach. *Annals of Biomedical Engineering*, **39**(10): pp. 2568–2583.

[29] Iraeus, J., Brynskog, E., *et al*. (2024) Development of SAFER HBM v11. *Chalmers digital repository https://research.chalmers.se/publication/544460*, 2024. 2024:06, Version 1.1.

[30] Snyder, R. G. (1975) Bioengineering study of basic physical measurements related to susceptibility to cervical hyperextension-hyperflexion injury. Final report. 1975.

[31] Reed, M. P. and Jones, M. L. (2017) A parametric model of cervical spine geometry and posture. Transportation Research Institute: University of Michigan, Ann Arbor, USA.

[32] Panjabi, M. M., Oxland, T., *et al*. (1993) Articular facets of the human spine quantitative three-dimensional anatomy. *Spine*, **18**(10): pp. 1298–1310.

[33] Pal, G. P., Routal, R. V., Saggu, S. K. (2001) The orientation of the articular facets of the zygapophyseal joints at the cervical and upper thoracic region. *Journal of Anatomy*, **198**(4): pp. 431–441.

[34] Womack, W., Ayturk, U. M., Puttlitz, C. M. (2010) Cartilage Thickness Distribution Affects Computational Model Predictions of Cervical Spine Facet Contact Parameters. *Journal of Biomechanical Engineering*, **133**(1).

[35] Panjabi, M. M., Chen, N. C., Shin, E. K., Wang, J.-L. (2001) The cortical shell architecture of human cervical vertebral bodies. *Spine*, **26**(22): pp. 2478–2484.

[36] Pitzen, T., Schmitz, B., *et al*. (2004) Variation of endplate thickness in the cervical spine. *European Spine Journal*, **13**(3): pp. 235–240.

[37] Raza, A., Howell, G. T., Michalek, A. J. (2024) Three-dimensional fiber patterning in the annulus fibrosus can be derived from vertebral endplate topography. *JOR Spine*, **7**(3): p. e1361.

[38] Mercer, S. and Bogduk, N. (1999) The Ligaments and Anulus Fibrosus of Human Adult Cervical Intervertebral Discs. *Spine*, **24**(7): pp. 619–626.

[39] Frost, B. A., Camarero-Espinosa, S., Foster, E. J. (2019) Materials for the Spine: Anatomy, Problems, and Solutions. *Materials*, **12**(2): p. 253.

[40] Pooni, J., Hukins, D., Harris, P., Hilton, R., Davies, K. (1986) Comparison of the structure of human intervertebral discs in the cervical, thoracic and lumbar regions of the spine. *Surgical and Radiologic Anatomy: SRA*, **8**(3): pp. 175–182.

[41] Yoganandan, N., Kumaresan, S., Pintar, F. A. (2000) Geometric and mechanical properties of human cervical spine ligaments. *Journal of Biomechanical Engineering*, **122**(6): pp. 623–629.

[42] Iraeus, J., Poojary, Y. N., Jaber, L., John, J., Davidsson, J. (2023) A new open-source finite element lumbar spine model, its tuning and validation, and development of a tissue-based injury risk function for compression fractures. *Nucleus*, **3**: p. 4.

[43] Holzapfel, G. A., Schulze-Bauer, C. A., Feigl, G., Regitnig, P. (2005) Single lamellar mechanics of the human lumbar anulus fibrosus. *Biomechanics and Modeling in Mechanobiology*, **3**: pp. 125–140.

[44] Buchweitz, N., Sun, Y., *et al*. (2025) Characterizing the Baseline Regional Biphasic Mechanical Properties of Cervical Intervertebral Discs. *Annals of Biomedical Engineering*. **53**(9): pp. 2333–2345.

[45] Hori, R. Y. and Mockros, L. (1976) Indentation tests of human articular cartilage. *Journal of Biomechanics*, **9**(4): pp. 259–268.

[46] Kopperdahl, D. L., Morgan, E. F., Keaveny, T. M. (2002) Quantitative computed tomography estimates of the mechanical properties of human vertebral trabecular bone. *Journal of Orthopaedic Research*, **20**(4): pp. 801–805.

[47] Ulrich, D., Van Rietbergen, B., Laib, A., Ruegsegger, P. (1999) The ability of three-dimensional structural indices to reflect mechanical aspects of trabecular bone. *Bone*, **25**(1): pp. 55–60.

[48] Hadagali, P. and Cronin, D. S. (2022) Enhancing the Biofidelity of an Upper Cervical Spine Finite Element Model Within the Physiologic Range of Motion and Its Effect on the Full Ligamentous Neck Model Response. *Journal of Biomechanical Engineering*, **145**(1).

[49] Jonas, R., Demmelmaier, R., Wilke, H. J. (2020) Influences of functional structures on the kinematic behavior of the cervical spine. *The Spine Journal*, **20**(12): pp. 2014–2024.

[50] Panjabi, M. M., Crisco, J. J., *et al*. (2001) Mechanical properties of the human cervical spine as shown by three-dimensional load-displacement curves. *Spine*, **26**(24): pp. 2692–2700.

[51] Wheeldon, J. A., Pintar, F. A., Knowles, S., Yoganandan, N. (2006) Experimental flexion/extension data corridors for validation of finite element models of the young, normal cervical spine. *Journal of Biomechanics*, **39**(2): pp. 375–380.

[52] Nightingale, R. W., Chancey, V. C., *et al*. (2007) Flexion and extension structural properties and strengths for male cervical spine segments. *Journal of Biomechanics*, **40**(3): pp. 535–542.

[53] Barrey, C., Rousseau, M. A., *et al*. (2015) Relevance of using a compressive preload in the cervical spine: an experimental and numerical simulating investigation. *European Journal of Orthopaedic Surgery and Traumatology*, **25**(Suppl 1): pp. S155–165.

[54] van Mameren, H., Sanches, H., Beursgens, J., Drukker, J. (1992) Cervical Spine Motion in the Sagittal Plane II: Position of Segmental Averaged Instantaneous Centers of Rotation - A Cineradiographic Study. *Spine*, **17**(5).

[55] Östh, J., Mendoza-Vazquez, M., *et al*. (2017) A female head–neck model for rear impact simulations. *Journal of Biomechanics*, **51**: pp. 49–56.

[56] Hueston, S. (2011) Anthropometric analysis of the cervical spine. Wright State University.

[57] Tonetti, J., Potton, L., *et al*. (2005) Morphological cervical disc analysis applied to traumatic and degenerative lesions. *Surgical and Radiological Anatomy*, **27**(3): pp. 192–200.

[58] Rong, X., Liu, Z., Wang, B., Chen, H., Liu, H. (2017) The facet orientation of the subaxial cervical spine and the implications for cervical movements and clinical conditions. *Spine*, **42**(6): pp. E320–E325.

[59] John, J. D., Yoganandan, N., Arun, M. W. J., Saravana Kumar, G. (2018) Influence of morphological variations on cervical spine segmental responses from inertial loading. *Traffic Injury Prevention*, **19**(sup1): pp. S29–S36.

[60] Bredbenner, T. L., Eliason, T. D., *et al*. (2014) Development and Validation of a Statistical Shape Modeling-Based Finite Element Model of the Cervical Spine Under Low-Level Multiple Direction Loading Conditions. *Frontiers in Bioengineering and Biotechnology*, **2**.

[61] Clogenson, M., Duff, J. M., *et al*. (2015) A statistical shape model of the human second cervical vertebra. *International Journal of Computer Assisted Radiology and Surgery*, **10**(7): pp. 1097–1107.

[62] Nissan, M. and Gilad, I. (1984) The cervical and lumbar vertebrae—an anthropometric model. *Engineering in Medicine*, **13**(3): pp. 111–114.

[63] Panjabi, M. M., Duranceau, J., Goel, V., Oxland, T., Takata, K. (1991) Cervical human vertebrae quantitative three-dimensional anatomy of the middle and lower regions. *Spine*, **16**(8): pp. 861–869.

[64] Bertrand, S., Skalli, W., *et al*. (2006) External and internal geometry of European adults. *Ergonomics*, **49**(15): pp. 1547–1564.

[65] Vasavada, A. N., Danaraj, J., Siegmund, G. P. (2008) Head and neck anthropometry, vertebral geometry and neck strength in height-matched men and women. *Journal of Biomechanics*, **41**(1): pp. 114–121.

[66] Busscher, I., Ploegmakers, J. J. W., Verkerke, G. J., Veldhuizen, A. G. (2010) Comparative anatomical dimensions of the complete human and porcine spine. *European Spine Journal*, **19**(7): pp. 1104–1114.

[67] Masharawi, Y., Rothschild, B., *et al*. (2004) Facet orientation in the thoracolumbar spine: three-dimensional anatomic and biomechanical analysis. *Spine*, **29**(16): pp. 1755–1763.

[68] Griffith, J. F. and Lee, J. C. (2024) Developmental cervical spinal canal size: population reference range. *Quantitative Imaging in Medicine and Surgery*, **14**(4): p. 3044.

[69] Ebraheim, N. A., Patil, V., Liu, J., Haman, S. P., Yeasting, R. A. (2008) Morphometric analyses of the cervical superior facets and implications for facet dislocation. *International Orthopaedics*, **32**(1): pp. 97–101.

[70] Panjabi, M. M., Shin, E. K., Chen, N. C., Wang, J.-L. (2000) Internal Morphology of Human Cervical Pedicles. *Spine*, **25**(10): pp. 1197–1205.

[71] Liu, Y. K., Krieger, K. W., *et al*. (1982) Cervical spine stiffness and geometry of the young human male. *Wright-Patterson Air Force Base, OH: Air Force Medical Research Laboratory*, pp. 1–97.

VIII. APPENDIX

A. Cervical *Spine FE Model Geometry*

A literature review of anatomical and biomechanical studies relevant to cervical spine geometry was conducted. The search was initiated in Google Scholar using keywords related to cervical spine anatomy, morphology, and geometric measurements. Publications identified served as starting points for further searches, in which both reference lists and citing works were reviewed to identify additional relevant publications.

1) Global Geometry Parameters

The inclusion–exclusion criteria used to select studies for the global geometry parameters were as follows.

- Sources measuring dry specimens were excluded.
- Sources without male cervical vertebra geometry information were excluded.
- Sources measuring geometry from fresh/frozen disarticulated specimens, CT/MRI on PMHS and CT/MRI on volunteers were included.
- Only data sources reporting the origin of the specimens were included.
- Only sources with details on the measurement method were included.

TABLE AI
DATA SOURCES AFTER INCLUSION–EXCLUSION SCREENING FOR THE GLOBAL GEOMETRY PARAMETERS
EXCLUDED STUDIES NOT INCLUDED IN THE PAPER REFERENCE LIST FOR BREVITY

Source	Age (years)	Average Height (cm)	Average Weight (kg)	Specimens (% males)	Measuring technique
Included					
Gilad and Nissan 1984, 1985, 1986 [62]	26.8	174.7	-	141 (100)	Lateral X-rays
Panjabi *et al*., 1991 [63]	46.3	167.8	67.8	12 (66)	CMM
Bertrand *et al*., 2006 [64]	30.3 ± 11.1	179.6 ± 6.2	76.1 ± 5.9	48 (100)	X-rays
Vasavada *et al*. 2008 [65]	25.8 ± 5.3	169 ± 3	74 ± 9	35 (100)	X-rays
Busscher *et al*., 2010 [66]	72	182	-	6 (100)	CT scans
Masharawi *et al*., 2021 [67]	30.7 ± 6.9	188 ± 7.5	83.8 ± 9.2	20 (100)	CT scans
Griffith *et al*., 2024 [68]	55 ± 17.4	166.6 ± 8.8	64.3 ± 13.3	256 (100)	CT scans
Excluded					
Francis 1955[a]	25–36	-	-	328 (100)	Vernier calipers
Katz *et al*.,1975[b]	18–24	164		30 (100)	X-rays
Przybylski *et al*., 1998[c]	58–95	-	-	20 (30)	Micrometer
Lu *et al*., 1999[d]	67.8	-	-	20(40)	Vernier calipers
Panjabi *et al*., 2001[e]	-	-	-	21 (-)	X-rays
Hukuda *et al*., 2002[f]	-	-	-	105 (100)	X-rays
Wandee *et al*., 2010[g]	52.4 ± 11	-	66.9 ± 10	30 (100)	MRI
Soo *et al*., 2016[h]	40.6	176.9	-	25 (100)	CT scans
Sheng *et al*., 2016[i]	30–40	-	60 - 80	12 (-)	Vernier calipers
Yu, Yan *et al*. 2019[j]	40.3 ± 10.9	-	-	10 (60)	MRI
Ye *et al*., 2023[k]	39.6 ± 4.8	-	-	30 (100)	CT scans

[a] Francis, C.C. (1955) 'Dimensions of the cervical vertebrae', *The Anatomical Record*, **122**(4), pp. 603–609.
[b] Katz, P.R., Reynolds, H.M., Foust, D.R. and Baum, J.K. (1975) 'Mid-sagittal dimensions of cervical vertebral bodies', *American Journal of Physical Anthropology*, **43**(3), pp. 319–326.
[c] Przybylski, G.J., Patel, P.R., Carlin, G.J. and Woo, S.L.-Y. (1998) 'Quantitative anthropometry of the subatlantal cervical longitudinal ligaments', *Spine*, **23**(8), pp. 893–898.
[d] Lu, J., Ebraheim, N., Yang, H., Rollins, J. and Yeasting, R. (1999) 'Anatomic bases for anterior spinal surgery: surgical anatomy of the cervical vertebral body and disc space', *Surgical and Radiologic Anatomy*, **21**(4), pp. 235.
[e] Panjabi, M.M., Chen, N.C., Shin, E.K. and Wang, J.-L. (2001) 'The cortical shell architecture of human cervical vertebral bodies', *Spine*, **26**(22), pp. 2478–2484.
[f] Hukuda, S. and Kojima, Y. (2002) 'Sex discrepancy in the canal/body ratio of the cervical spine implicating the prevalence of cervical myelopathy in men', *Spine*, **27**(3), pp. 250–253.
[g] Wandee, U., Itiravivong, P., Tejapongvorachai, T. and Tangpornprasert, P. (2010) 'Cervical disc dimensions of the Thai population', *Chulalongkorn Medical Journal*, **54**(3), pp. 225–236.

[h] Soo, A.E., Olsson, E. and Lim, M. (2016) 'Prediction of cervical endplate size: one size does not fit all', *Orthopedics*, **39**(3), pp. e526–e531.

[i] Sheng, S.-R., Xu, H.-Z., *et al.* (2016) 'Comparison of cervical spine anatomy in calves, pigs and humans', *PLoS One*, **11**(2), pp. e0148610.

[j] Yu, Y., Li, J.-S., *et al.* (2019) 'Normal intervertebral segment rotation of the subaxial cervical spine: an in vivo study of dynamic neck motions', *Journal of Orthopaedic Translation*, **18**, pp. 32–39.

[k] Ye, S.-q., Zhao, L.-j., *et al.* (2023) 'Measurement of anatomical parameters of anterior transpedicular root screw intervertebral fusion system of cervical spine', *BMC Musculoskeletal Disorders*, **24**(1), pp. 905.

TABLE AII
GLOBAL GEOMETRY PARAMETERS: DEFINITIONS, LITERATURE SUMMARIES (REPRESENTED USING BAR PLOTS), AND SCHEMATIC ILLUSTRATIONS ON THE IMPLEMENTATION IN THE FE MODEL

Parameter	Literature summary	Illustration (representative parameter shown in red)
Anterior vertebra body superior–inferior height In the FE model, this measure corresponds to the distance between the extreme nodes in the superior–inferior direction at the anterior region of the vertebral body.	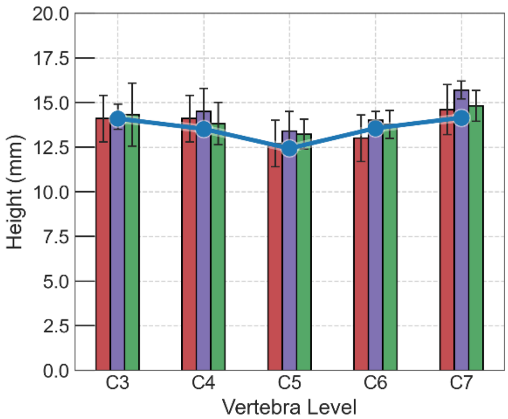	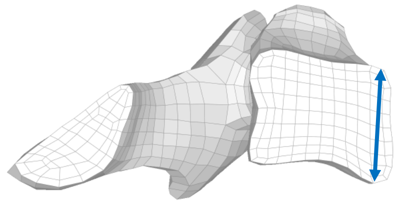
Posterior vertebra body superior–inferior height The distance between the extreme nodes on the posterior wall of the vertebral body in the superior–inferior direction within the mid-sagittal plane.	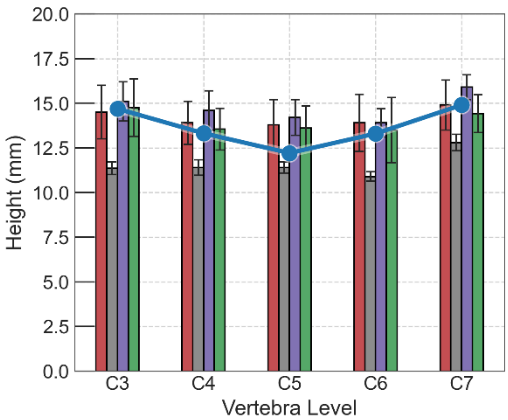	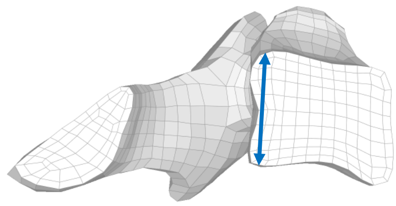
Vertebra body centre superior–inferior height The distance between the extreme nodes at the centre of the vertebral body in the superior–inferior direction within the mid-sagittal plane.	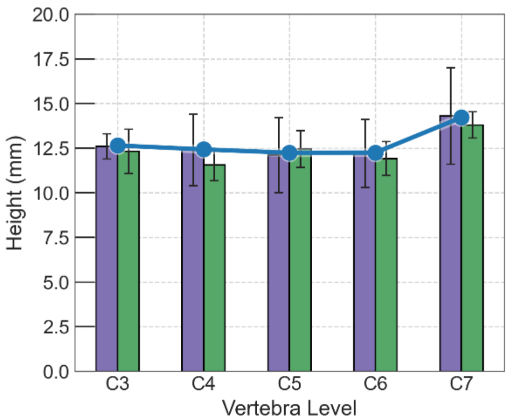	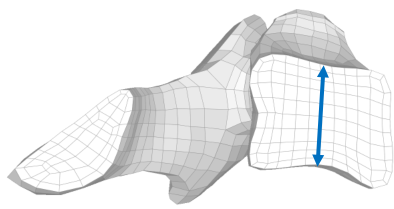
Bar plot common legend **The blue line (Baseline) in the plot is the resulting measures in the FE model.*	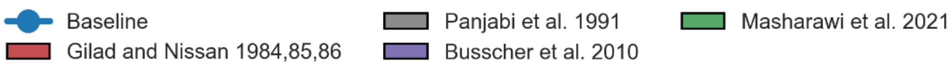	

Vertebra body anterior–posterior depth (Superior)
The distance between the extreme nodes at the centre of the vertebral body in the anterior–posterior direction, defined in both the mid-sagittal and transverse planes.

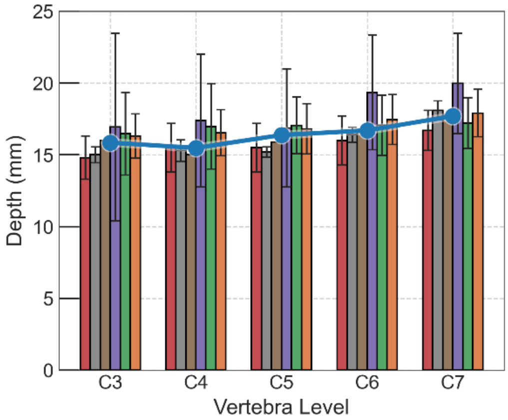

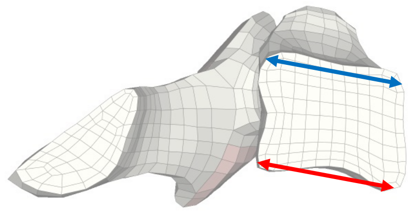

Vertebra in mid-sagittal plane. Blue: superior depth, and red: inferior depth

Vertebra body anterior–posterior depth (Inferior)
Similar to the previous, but at the inferior end.

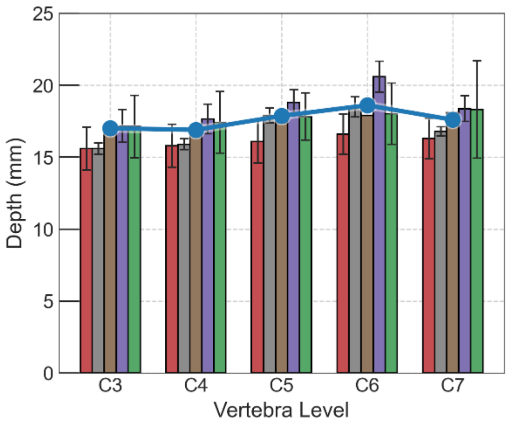

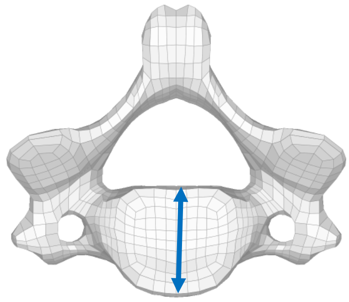

Vertebra in transverse plane. Red: inferior depth (represents same dimension as red in the above image).

Vertebra body medial–lateral width (Superior-endplate)
This measure corresponds to the distance between the extreme nodes of the endplate (not including the uncovertebral cleft) in the medial–lateral direction, defined in both the frontal and transverse planes.

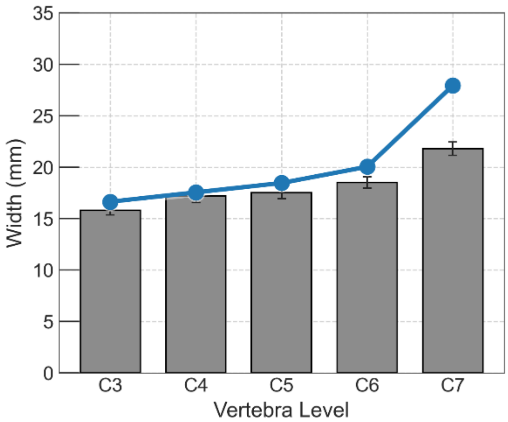

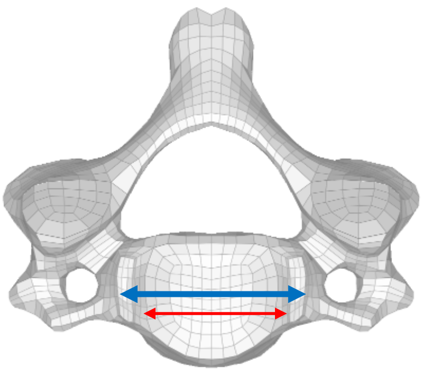

Vertebra body medial–lateral width (Superior)
This measure corresponds to the distance between the extreme nodes of the vertebra. Similar to previous plus the uncovertebral clefts.

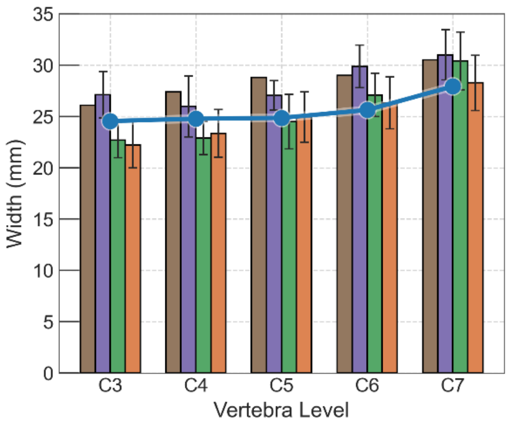

Vertebra in transverse plane.

Red: superior endplate vertebra body medial–lateral width.

Blue: superior vertebra body medial–lateral width (includes the uncovertebral cleft).

Bar plot common legend
** The blue line (Baseline) in the plot is the resulting measures in the FE model.*

Baseline
Gilad and Nissan 1984,85,86
Panjabi et al 1991
Bertrand et al. 2006
Busscher et al. 2010
Masharawi et al. 2021
Griffith 2024

Vertebra body medial–lateral width (Inferior)
Similar to the previous measure in the inferior end (uncovertebral clefts not applicable for this measure).

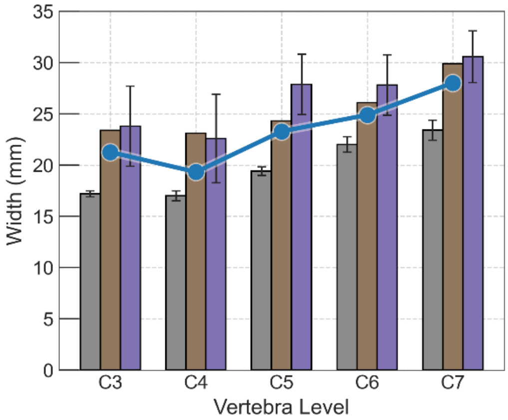

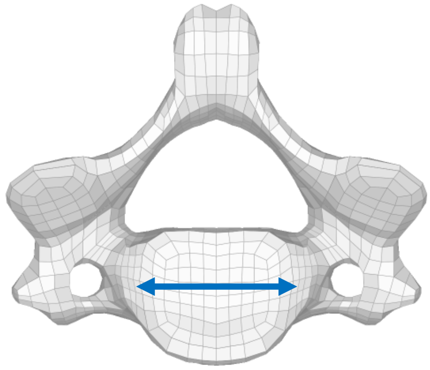

Disc centre superior–inferior height
The distance between the central nodes of the cranial and caudal endplates with respect to the intervertebral disc. The distance is defined in the superior–inferior direction within the mid-sagittal plane.

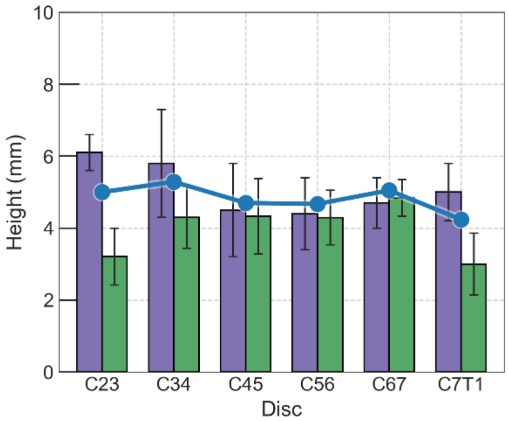

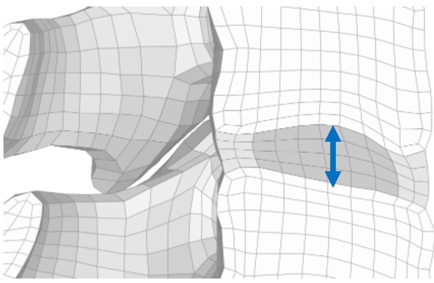

Vertebra canal anterior–posterior depth
The anterior–posterior distance between the nodes located within the vertebral canal in the transverse plane.

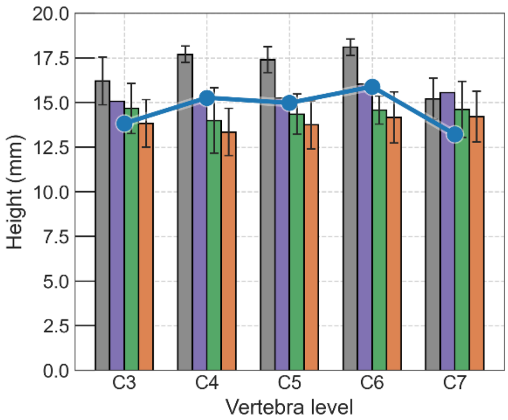

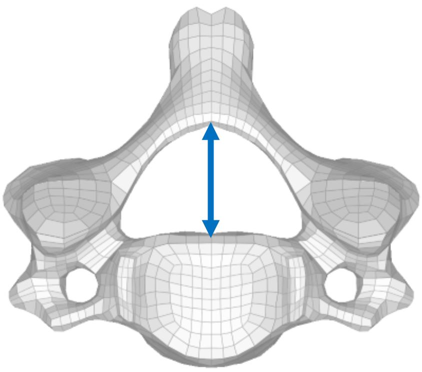

Vertebra canal medial–lateral width
Similarly, this measure corresponds to the medial–lateral distance, defined in the transverse plane.

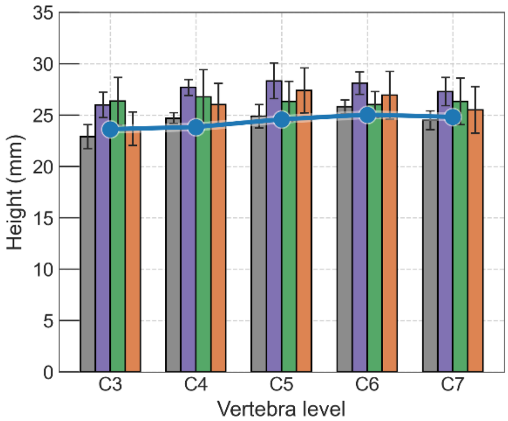

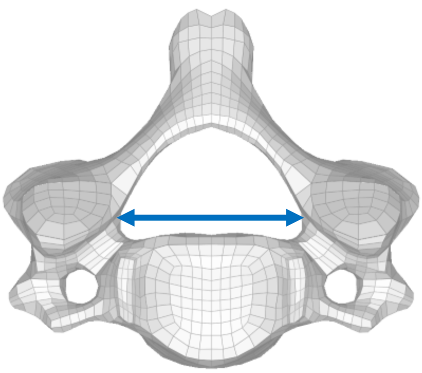

Bar plot common legend
** The blue line (Baseline) in the plot is the resulting measures in the FE model.*

Baseline
Panjabi et al 1991
Bertrand et al. 2006
Busscher et al. 2010
Masharawi et al. 2021
Griffith et al. 2024

Average male cervical spine target geometries that were used for morphing the cervical spine model based on the summarised geometric data from Table AII are shown in the below table, Table AIII.

TABLE AIII
GLOBAL GEOMETRY TARGETS FOR INDIVIDUAL CERVICAL VERTEBRAE IN THE SAGITTAL AND TRANSVERSE PLANES

Vertebra	Transverse plane (Superior view)	Mid-Sagittal Plane	Transverse plane (Inferior view)
C3	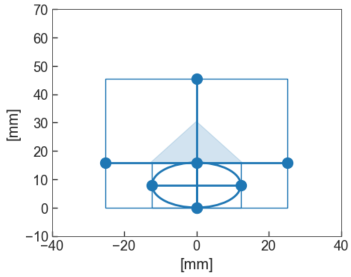	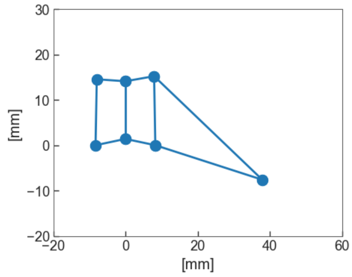	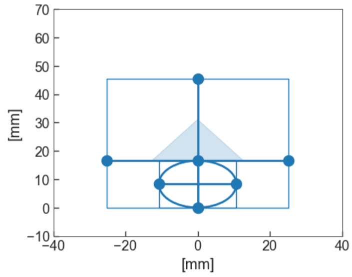
C4	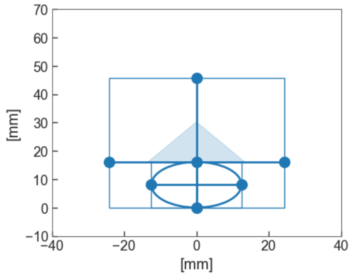	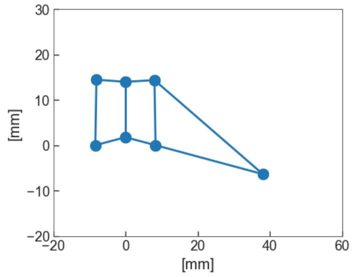	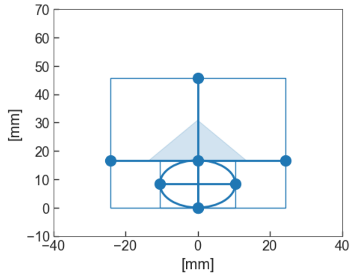
C5	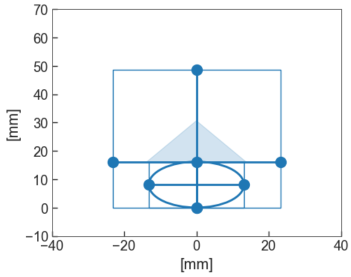	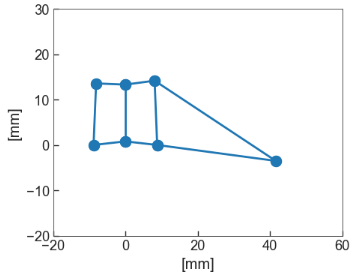	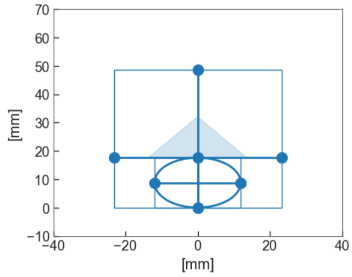
C6	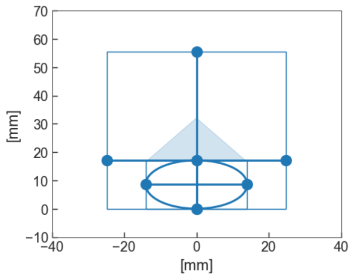	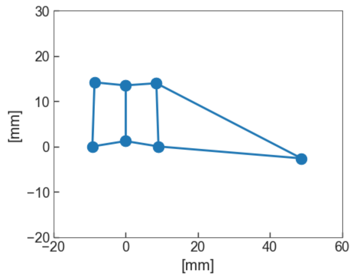	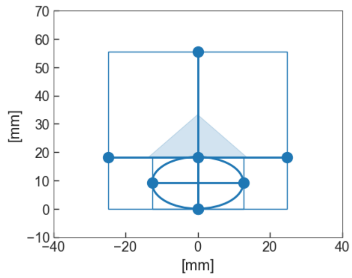
C7	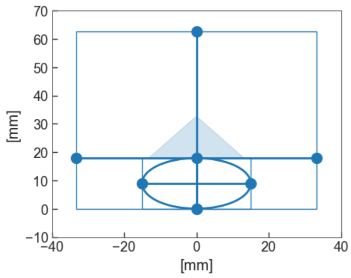	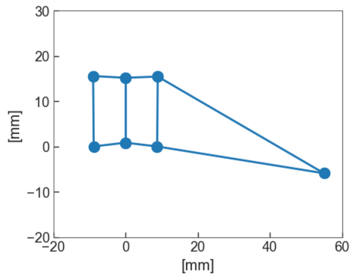	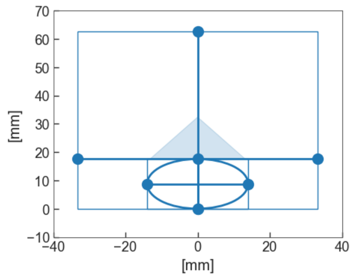

2) Local Geometry Parameters

Due to limited data availability for local geometry parameters, all identified studies were included, and no specific inclusion–exclusion criteria were defined.

TABLE AIV

DATA SOURCES FOR LOCAL CERVICAL GEOMETRY PARAMETERS AND THEIR USE IN GEOMETRY TARGET DEFINITION

Source	Age (years)	Specimens (% males)	Measuring technique	Specific parameter
Facets				
Panjabi *et al.*, 1993 [32]	46.3	84 (67)	Digital markers	Facet orientation and dimension
Pal, G. P., *et al.*, 2001 [33]	-	30 (100)	Physical	Facet orientation
Ebraheim, N. A., *et al.*, 2008 [69]	56	30 (60)	Physical	Facet orientation
Rong, X., *et al.*, 2017 [58]	46.26	100 (58)	CT	Facet orientation
Cortical thickness				
Panjabi *et al.*, 2000 [70]	-	25 (-)	X-rays	Pedicles
Panjabi *et al.*, 2001 [35]	-	21 (-)	X-rays	Anterior and posterior walls
Pitzen, T., *et al.*, 2004 [36]	62.7 ± 7.5	6 (-)	CT*	Endplate
Annulus Fibers				
Raza, A., *et al.*, 2024 [37]	-	-	CT	Fiber orientation (for lumbar spine)
Frost, B. A., *et al.*, 2019 [39]	-	-	-	Fiber thickness (estimated)

** Data from CT were compensated using correction factors based on Silva, M. J., et al. (1994) [a].*

[a] Silva, M. J., Wang, C., Keaveny, T. M., and Hayes, W. C. (1994) Direct and computed tomography thickness measurements of the human, lumbar vertebral shell and endplate. *Bone*, **15**(4): pp. 409–414.

TABLE AV

LOCAL GEOMETRY PARAMETERS: DEFINITION, LITERATURE SUMMARY AND THE ILLUSTRATION OF THE IMPLEMENTATION IN FE MODEL

Parameter	Literature summary (Aggregate plotted as a red line)	Illustration (representative parameter shown in red)
Facet transverse angle (superior) Facet angle with respect to the transverse plane, obtained in the FE model by projecting the facet angle onto the vertebra-specific reference planes. The angle is influenced by the mesh discretisation in FE.	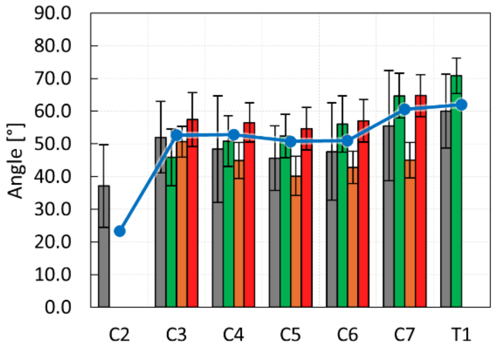	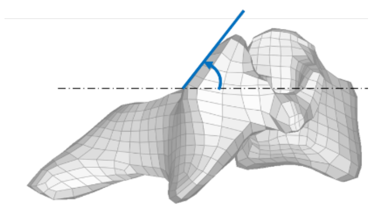
Facet transverse angle (inferior) Facet angle with respect to the transverse plane, obtained in the FE model by projecting the facet angle onto the vertebra-specific reference planes. The angle is influenced by the mesh discretisation in FE.	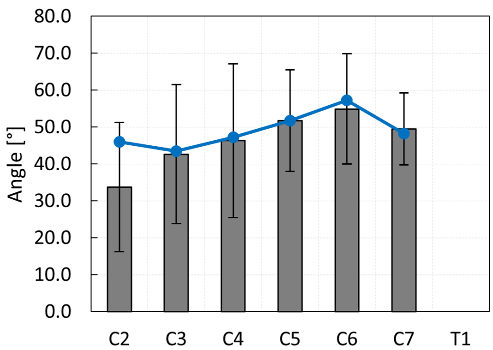	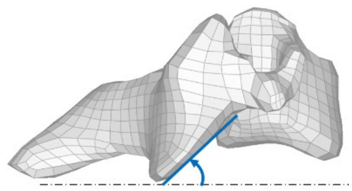
Bar plot common legend ** The blue line (Baseline) in the plot is the resulting measures in the FE model.*	Panjabi et al., 1993; Pal, G. P et al., 2001; Ebraheim, N. A., et al., 2008; Rong, X., et al. 2017; Baseline	

Facet sagittal angle (superior)

This corresponds to the facet angle with respect to the sagittal anatomical plane, obtained by projecting the angle onto the vertebra-specific reference plane.

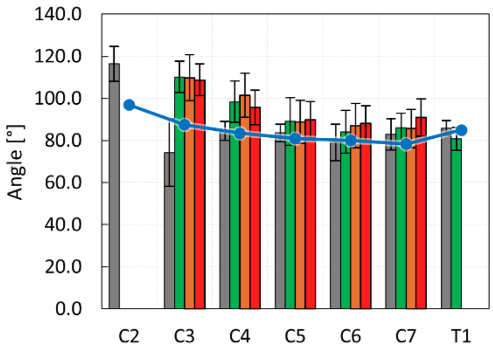

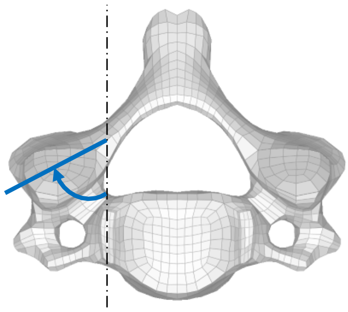

Facet sagittal angle (inferior)

Similar to the previous measure to the inferior facet.

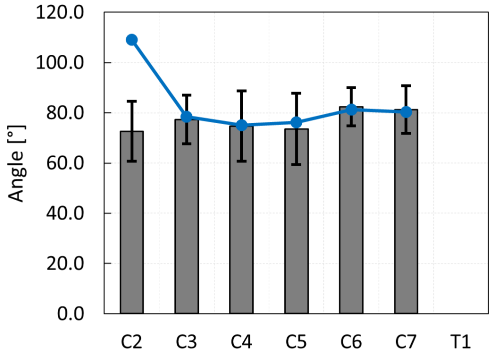

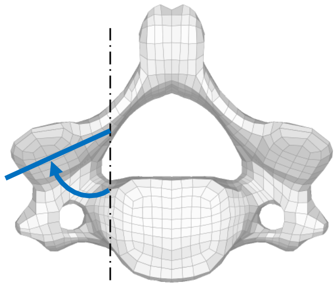

Bar plot common legend

** The blue line (Baseline) in the plot is the resulting measures in the FE model.*

Panjabi et al., 1993
Pal, G. P et al., 2001
Ebraheim, N. A., et al., 2008
Rong, X., et al. 2017
Baseline

FE Illustrations (below figures for C3)

Anterior cortical thickness

The anterior cortical thickness corresponds to the nodal thickness in mm assigned in the FE model. At each nodal location, the thickness value is obtained from literature data and linearly interpolated in ANSA.

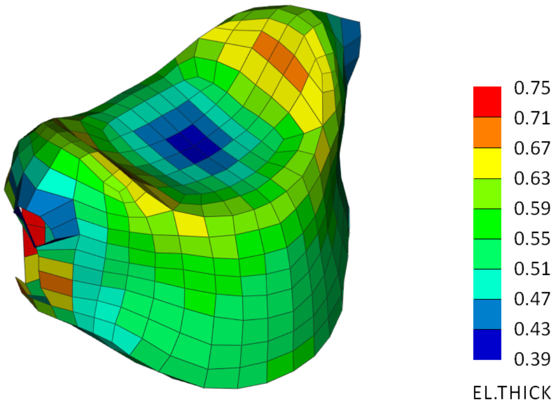

Posterior cortical thickness

A constant cortical thickness in mm is assigned to the posterior region in the FE model.

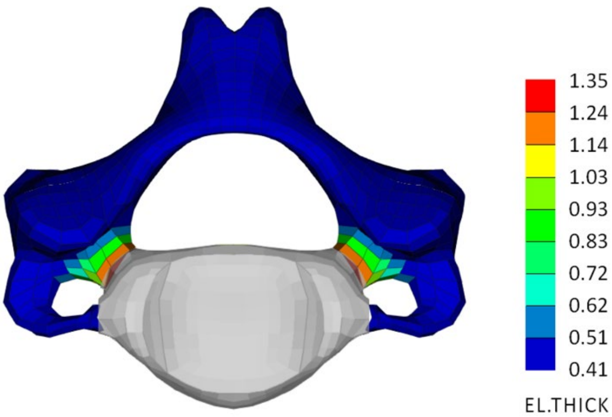

B. Calibration and Validation of the Intervertebral Disc

Reference [44] presents confined compression tests for annulus ground and nucleus samples from five male cadaveric cervical spines (mean age 59 ± 13 years). Raw data from these tests were used to fit an Ogden model in LS-DYNA under compression. Tensile properties were calibrated to provide minimal stiffness while maintaining model stability (Fig. B1).

To validate the developed IVD material models, the stiffness of a FSU was compared with physical axial compression tests reported in [71]. As no differences in response were observed across loading rates in the physical experiments, simulations were conducted at a single loading rate. The compressive validation showed that the FSU stiffness with calibrated materials fell within the range of reported experimental responses (Fig. B2).

The current IVD material tuning does not include rate dependency. Although the Ogden model in LS-DYNA can incorporate rate effects and relaxation data for both the annulus ground and nucleus are available in [44], direct incorporation into the material model increased disc stiffness in quasistatic tests. However, this approach may result in excessive flexibility at higher loading rates.

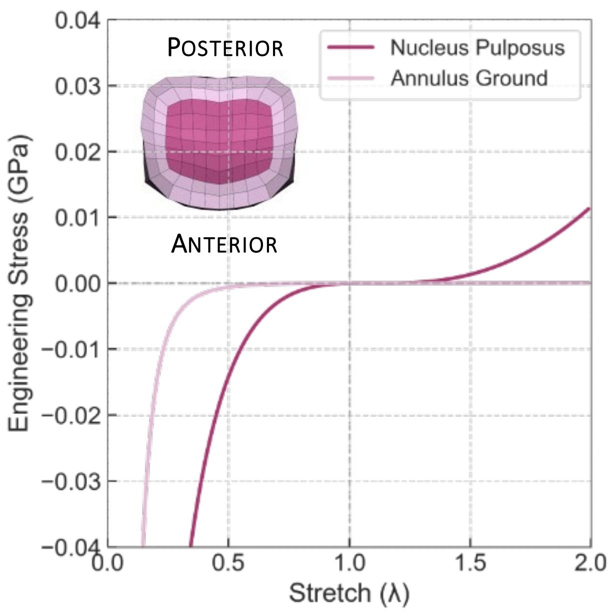

Fig. B1. Ogden material curves in LS-DYNA for annulus ground (light pink) and nucleus pulposus (dark pink). An example of the modelled cervical disc is shown in the top left, using the same colour scheme.

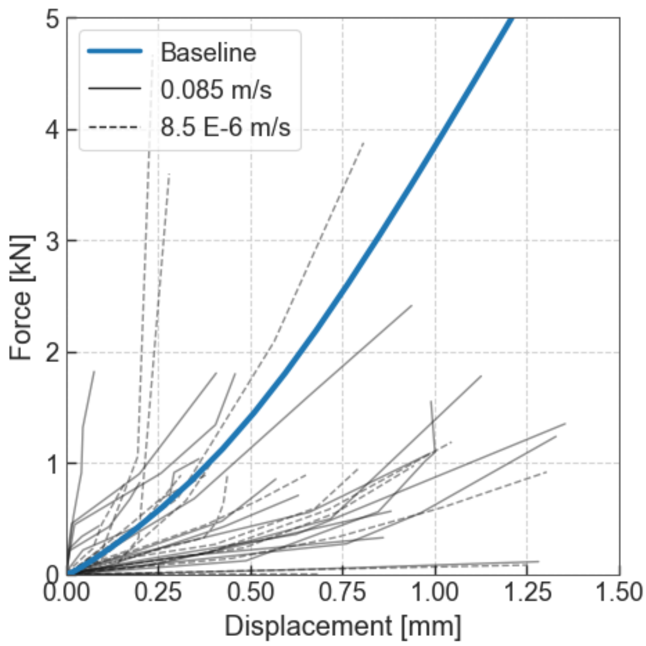

Fig. B2. Force-deflection response of C4-C5 FSU in axial compression compared to tests in [71].

C. Detailed results from ligament unstretched length calibration

TABLE CI
SUMMARY OF SLACKS RESULTING FROM CALIBRATION USING [49]

Ligament	FSUs levels		
	C2–C3 (%)	C4–C5 (%)	C6–C7 (%)
Anterior longitudinal ligament	0 (0)	0 (0)	0 (0)
Posterior longitudinal ligament	0 (0)	1 (23)	1 (22)
Capsular ligament	0 (0)	2 (44)	2 (54)
Ligament flavum	1 (14)	1 (12)	1 (10)
Intra spinous ligament	0 (0)	0 (0)	2 (17)

Slack values in mm and values inside bracket represents % of initial length from [24].

In Fig. C1-C7, the solid lines represent the simulation responses for each cervical segment, while the markers with error bars indicate the corresponding experimental test results [49]. A consistent colour scheme is used throughout all plots: green denotes the C2–C3 segment; red denotes the C4–C5 segment; and blue denotes the C6–C7 segment.

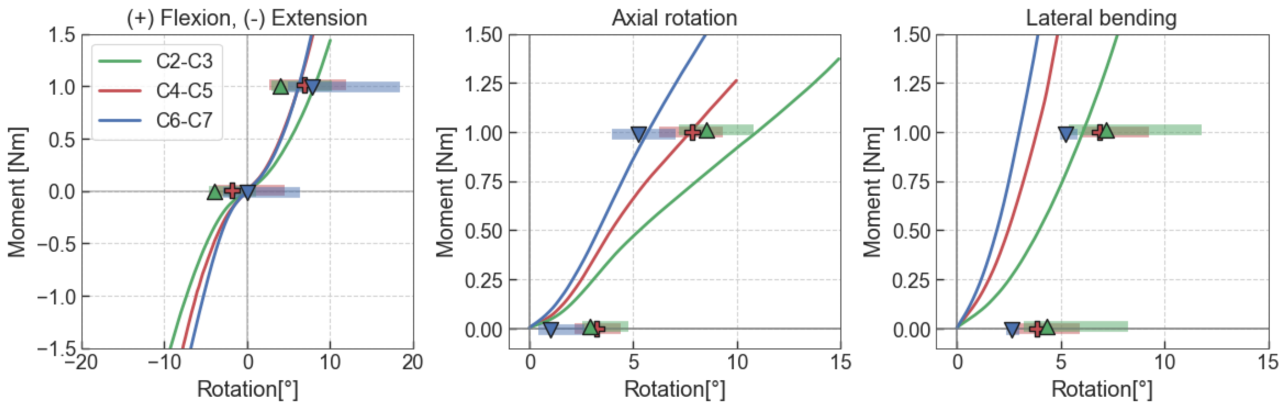

Fig. C1. Step 1 – calibration with isolated IVDs. Flexion responses of the FSUs match the reported test ranges. Axial rotation responses are within the test ranges for C4–C5 and C6–C7; while for C2–C3 they are at the upper limit. In lateral bending, stiffness is overestimated for C4–C5 and C6–C7, while for C2–C3 it is at the lower limit for the test range.

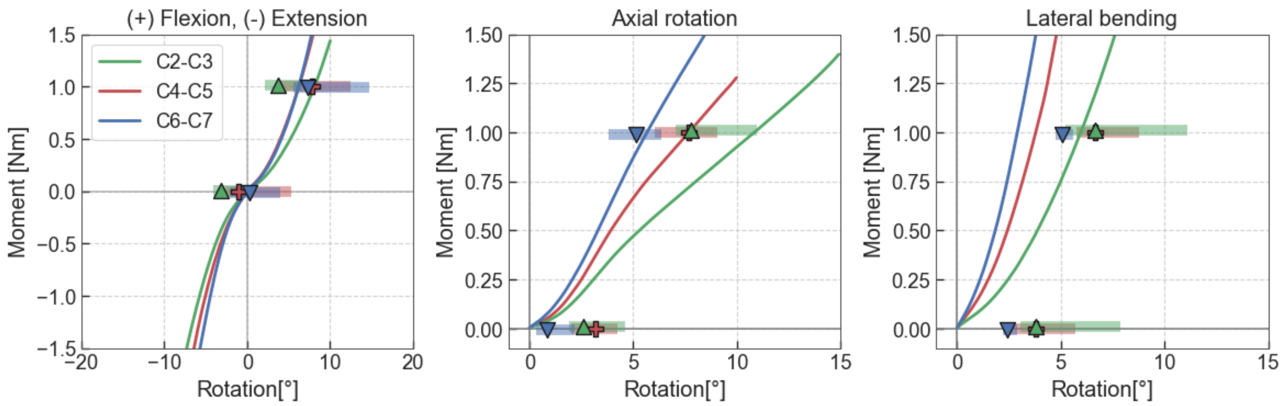

Fig. C2. Step 2 – calibration resulted in 0 mm slack for the Anterior Longitudinal Ligament (ALL) in all FSUs. Similar to Step 1, flexion responses match the reported test ranges. Axial rotation is within the test ranges for C4–C5 and C6–C7 and reaches the upper limit for C2–C3. In lateral bending, stiffness is overestimated for C4–C5 and C6–C7, whereas for C2–C3 it is at the lower limit of the test range.

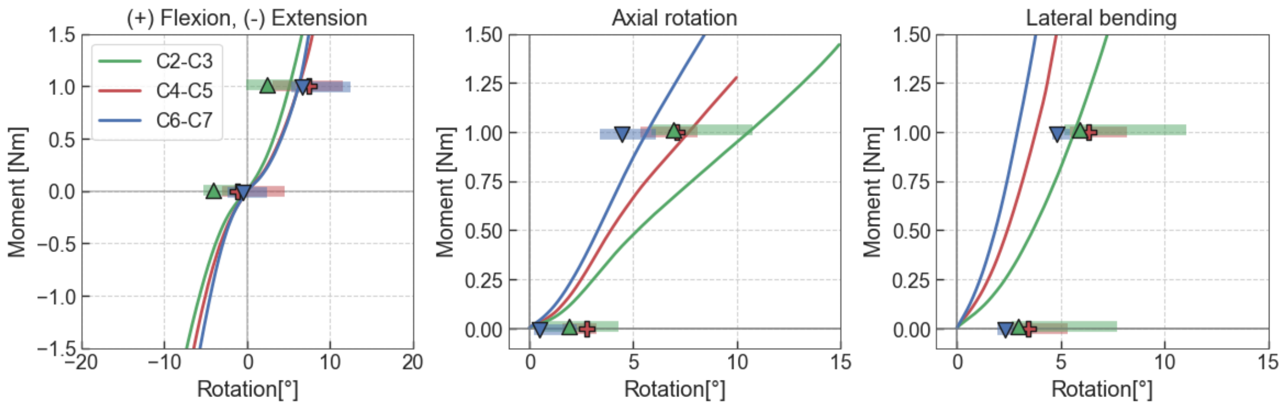

Fig. C3. Step 3 – calibration of the Posterior Longitudinal Ligament (PLL) resulted in +0 mm slack for C2–C3 and +1 mm slack for C4–C5 and C6–C7. Response behaviour was similar to Steps 1 and 2.

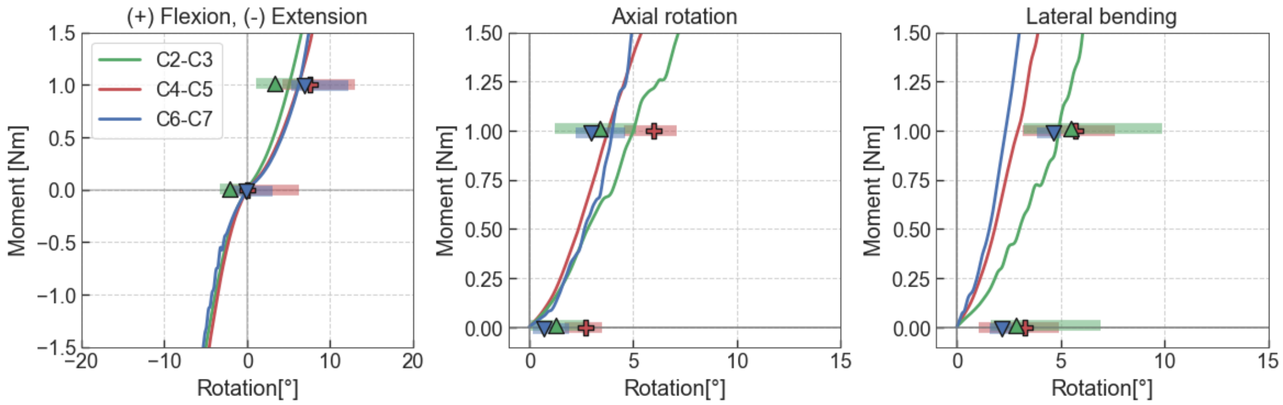

Fig. C4. Step 4 – adding of the Posterior Vertebral Body (PVB). This step resulted in a stiffer and noisy response in axial rotation compared to the previous steps due to contact definitions between the facet surfaces.

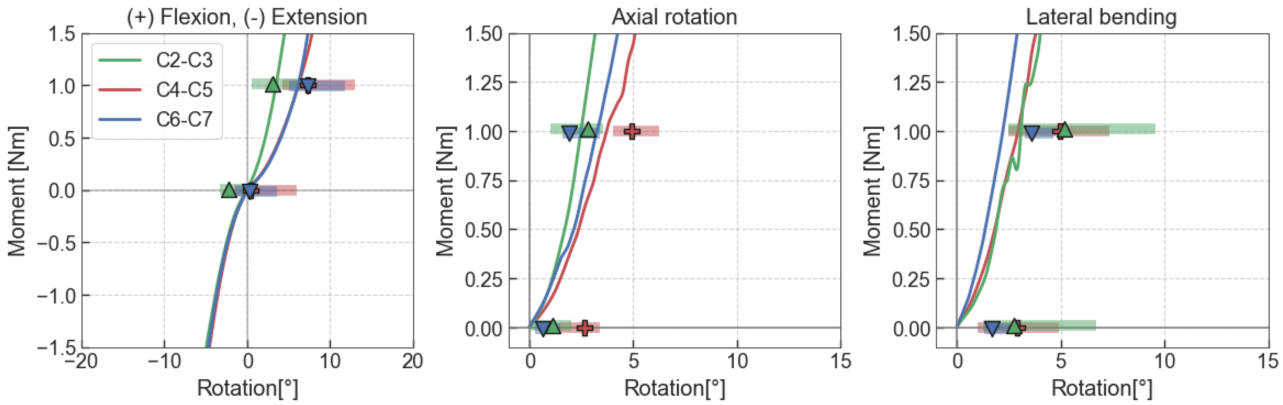

Fig. C5. Step 5 – calibration of the Capsular Ligament (CL) resulted in +0 mm slack for C2–C3 and +2 mm slack for C4–C5 and C6–C7.

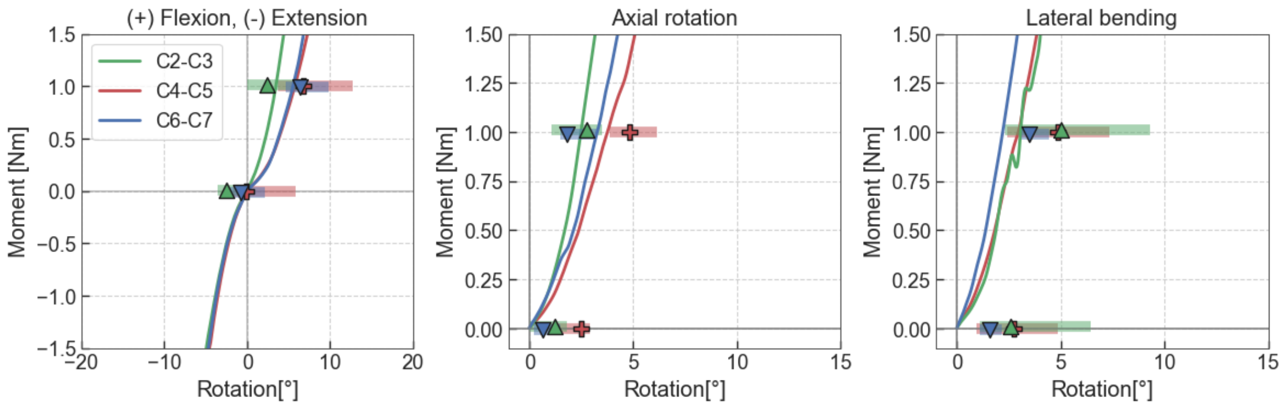

Fig. C6. Step 6 – calibration of the Ligament Flavum (LF) resulted in +1 mm slack for C2–C3, C4–C5 and C6–C7.

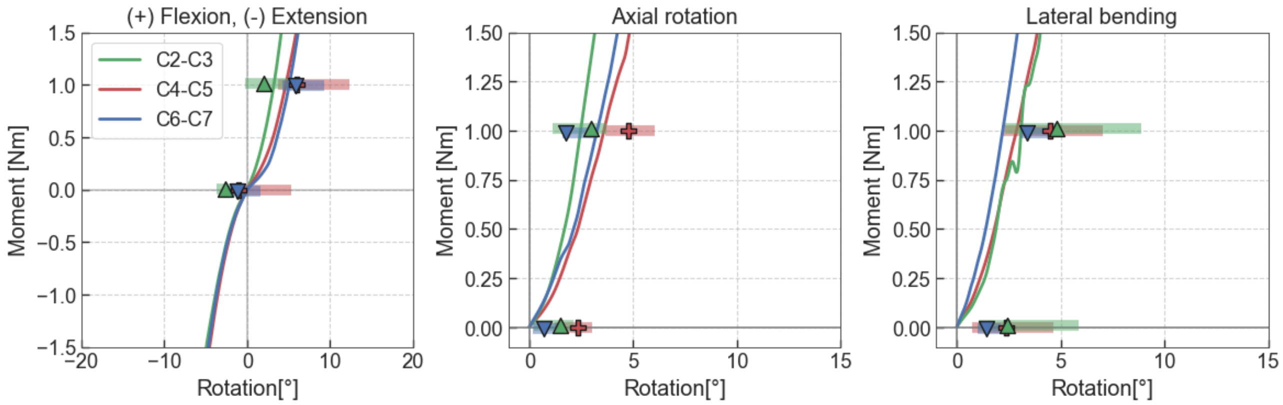

Fig. C7. Step 7 – calibration of the Intra Spinous Ligament (ISL) resulted in 0 mm slack for C2–C3 and C4–C5, and +2 mm slack for C6–C7.

D. *Detailed Validation results*

1) Range of motion

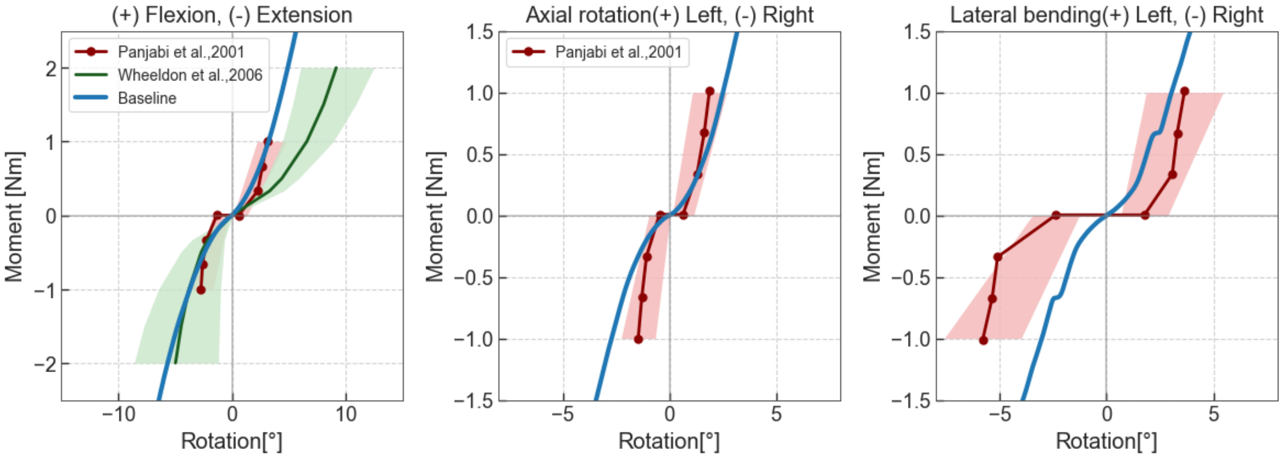

Fig. D1. Resulting validation of C2–C3 moment-rotation response, compared to [49-51]. *Note:* the axes limits used for flexion-extension are different from the other two plots.

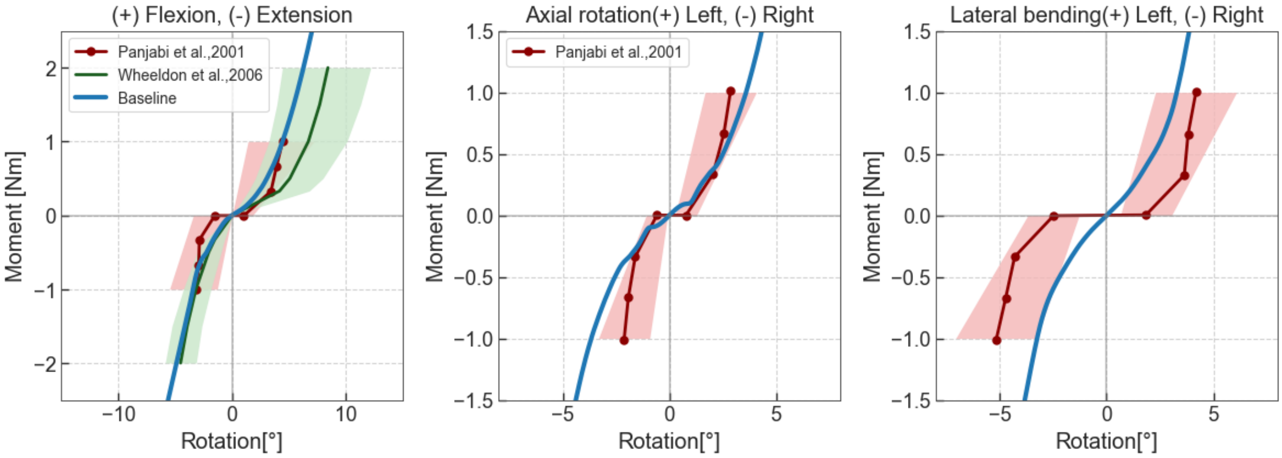

Fig. D2. Resulting validation of C3–C4 moment-rotation response, compared to [49-51]. *Note:* the axes limits used for flexion-extension are different from the other two plots.

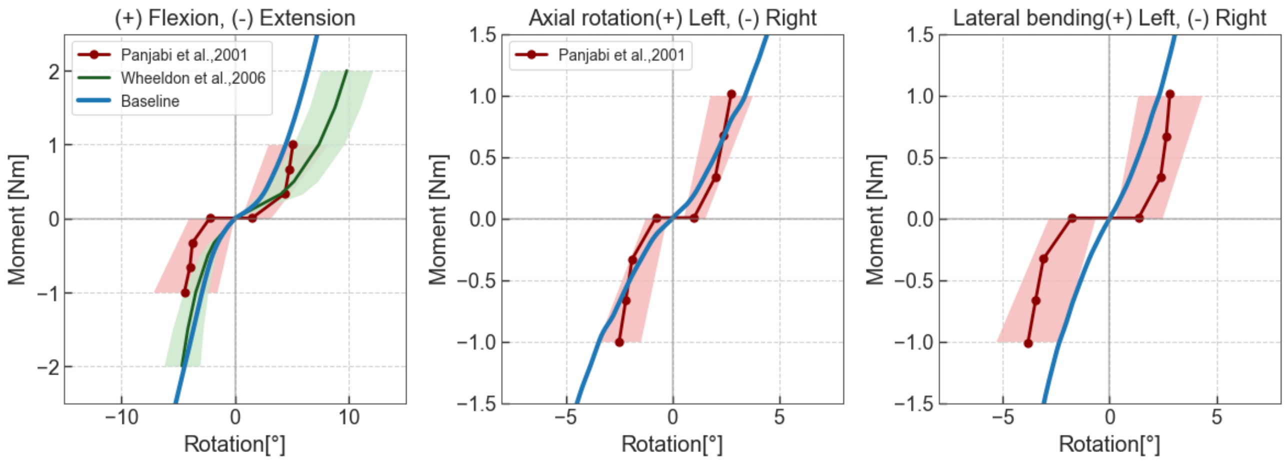

Fig. D3. Resulting validation of C5–C6 moment-rotation response, compared to [49-51]. *Note:* the axes limits used for flexion-extension are different from the other two plots.

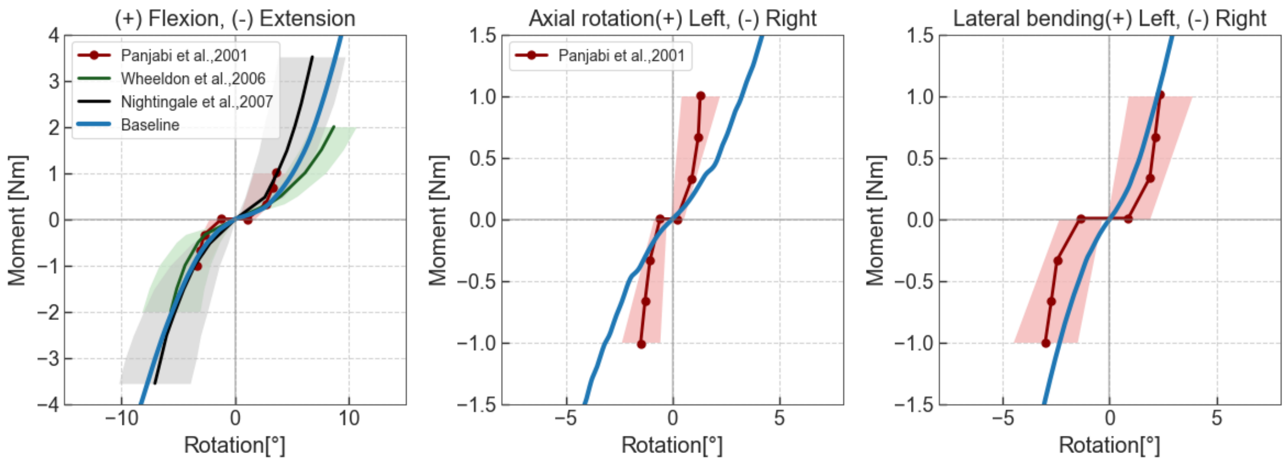

Fig. D4. Resulting validation of C6–C7 moment-rotation response, compared to [49-52]. *Note:* the axes limits used for flexion-extension are different from the other two plots.

2) Instantaneous Center of Rotation

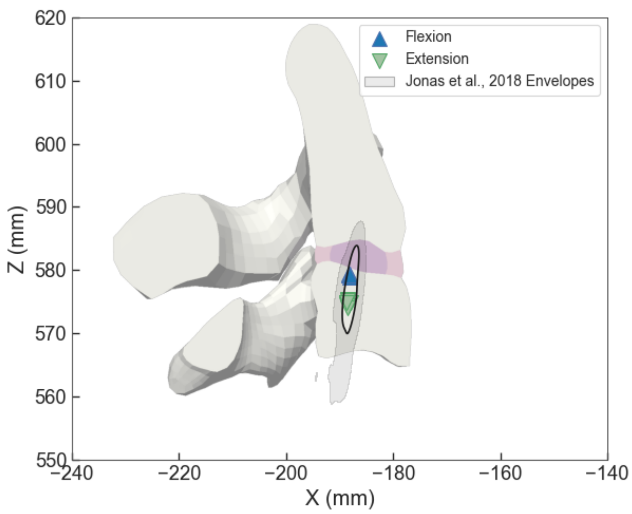

Fig. D5. Resulting segmental ICRs for C2–C3, blue markers (10 markers) representing ICRs in flexion (10 markers), green in extension. The black envelope shows the 50% HDR and the shaded grey envelope shows the 95% HDR from [26].

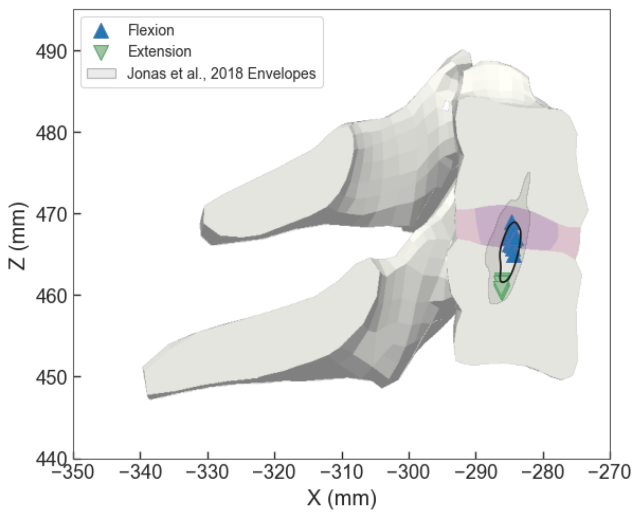

Fig. D6. Resulting segmental ICRs for C6–C7, blue markers (10 markers) representing ICRs in flexion (10 markers), green in extension. The black envelope shows the 50% HDR and the shaded grey envelope shows the 95% HDR from [26].

E. Vertebra Geometry and Ligament Material Population Variability Study

1) Ligament linear stiffness correlations from [24]

Pearson correlations were calculated for the linear region of ligament stiffness. Ligaments from a single FSU within an individual were treated as a “group”. Correlation values were categorised for visualisation: absolute values below 0.40 were considered low, values between 0.40 and 0.89 were considered moderate, and values between 0.90 and 1.00 were considered high. Negative correlations were indicated using a lighter shade of the same category. Correlations were calculated on both the whole dataset and the subset of male specimens.

The resulting correlation matrices did not reveal any clear trends. The combined dataset and the subset including only male specimens exhibited different correlation patterns among ligaments. Correlations of linear stiffness across ligaments at different loading rates indicated that variability in one ligament was independent of variability in others.

Quasi (0.5 s-1)														
MALES+ FEMALES								ONLY MALES						
	ALL	PLL	CL 1	CL 2	LF	ISL			ALL	PLL	CL 1	CL 2	LF	ISL
ALL	1.00							ALL	1.00					
PLL	0.35	1.00						PLL	0.52	1.00				
CL 1	0.59	0.52	1.00					CL 1	0.78	0.69	1.00			
CL 2	0.64	0.18	0.74	1.00				CL 2	0.86	-0.28	0.72	1.00		
LF	0.70	0.51	0.73	0.38	1.00			LF	0.93	0.71	0.87	0.94	1.00	
ISL	0.23	-0.13	0.03	0.25	0.46	1.00		ISL	0.26	-0.32	0.03	0.80	0.20	1.00

Fig. E1. Correlation matrix for quasistatic (0.5 s^{-1}) cervical spine ligament tests reported in [24]. The dataset includes 102 ligament specimens grouped into 16 groups across six unique cervical spine levels. Specimens were obtained from six unique PMHS, with samples from seven males and nine females.

Medium (20 s-1)														
MALES+ FEMALES								ONLY MALES						
	ALL	PLL	CL 1	CL 2	LF	ISL			ALL	PLL	CL 1	CL 2	LF	ISL
ALL	1.00							ALL	1.00					
PLL	0.48	1.00						PLL	0.32	1.00				
CL 1	0.04	-0.14	1.00					CL 1	-0.13	-0.41	1.00			
CL 2	0.18	-0.06	0.35	1.00				CL 2	0.00	-0.25	0.20	1.00		
LF	-0.15	-0.02	0.10	0.22	1.00			LF	-0.61	0.04	-0.06	0.03	1.00	
ISL	0.16	0.46	-0.22	-0.24	0.62	1.00		ISL	-0.25	0.46	-0.66	-0.52	0.57	1.00

Fig. E2. Correlation matrix for medium (20 s^{-1}) cervical spine ligament tests reported in [24]. The dataset includes 88 ligament specimens grouped into 13 groups across six unique cervical spine levels. Specimens were obtained from five unique PMHS, with samples from seven males and six females.

High (150 or 250 s-1)														
MALES+ FEMALES								ONLY MALES						
	ALL	PLL	CL 1	CL 2	LF	ISL			ALL	PLL	CL 1	CL 2	LF	ISL
ALL	1.00							ALL	1.00					
PLL	-0.38	1.00						PLL	-0.01	1.00				
CL 1	-0.40	0.18	1.00					CL 1	-0.33	-0.03	1.00			
CL 2	-0.26	-0.16	0.58	1.00				CL 2	-0.40	-0.16	0.67	1.00		
LF	0.24	-0.35	-0.17	0.26	1.00			LF	-0.23	0.20	-0.25	-0.30	1.00	
ISL	0.18	0.31	0.20	-0.04	0.03	1.00		ISL	0.24	0.73	-0.05	-0.64	-0.18	1.00

Fig. E3. Correlation matrix for high (150–250 s^{-1}) cervical spine ligament tests reported in [24]. The dataset includes 121 ligament specimens grouped into 19 groups across seven unique cervical spine levels. Specimens were obtained from six unique PMHS, with samples from nine males and nine females.

2) Visualisation of Population variability

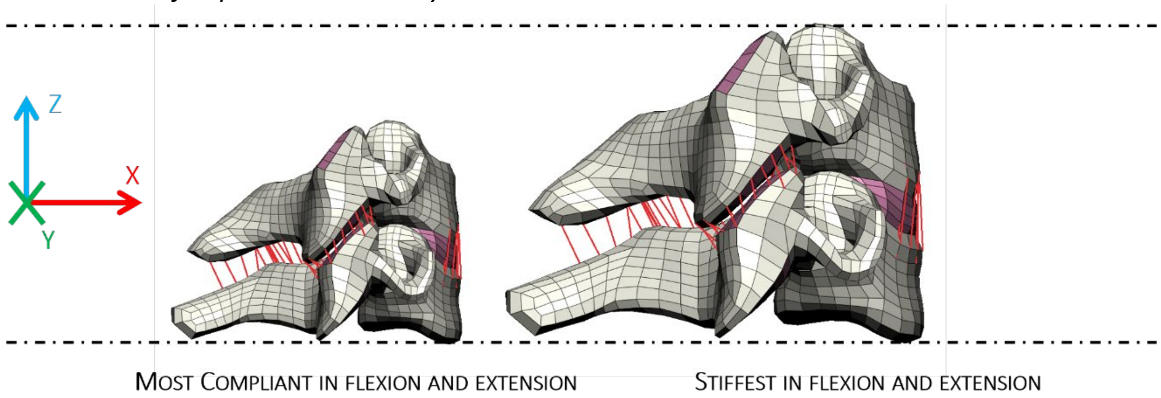

Fig. E4. Most compliant and stiffest FSU models in two-parameter group population study. Each model was generated by randomly sampling one geometry and one ligament material parameter. Differences in individual variation are shown in Table EI.

TABLE EI
VARIATIONS OF the models in Fig. E4

Variation Parameter	Most compliant (% change with respect to baseline)	Stiffest (% change with respect to baseline)
Geometry		
Global X	- 18%	+ 18%
Global Y	- 13%	+ 12%
Global Z	- 18%	+ 17%
Ligament	- 45%	+ 61 %

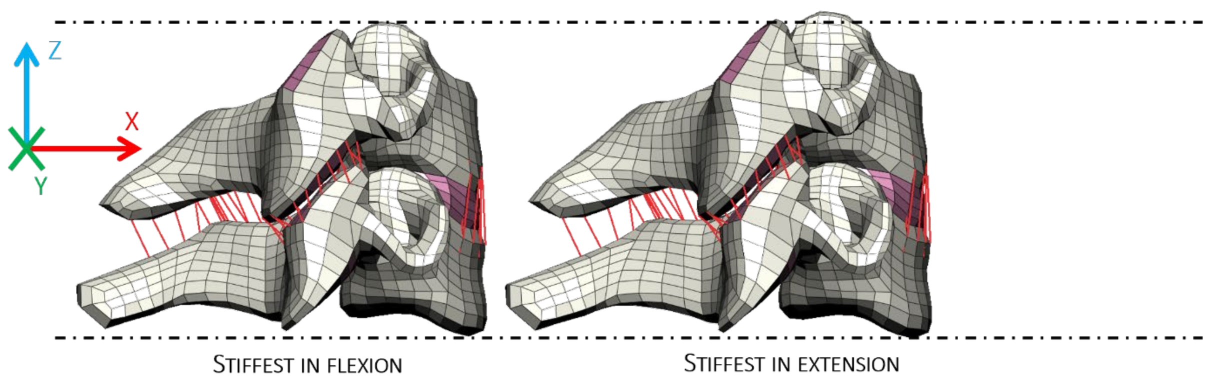

Fig. E5. Stiffest FSU models in flexion and extension models in six-parameter group population study. Differences in individual variation are shown in Table EII.

TABLE EII
VARIATIONS OF THE MODELS In Fig. E5

Variation Parameter	Stiffest In Flexion (% change with respect to baseline)	Stiffest In Extension (% change with respect to baseline)
Geometry		
Global X	+ 18%	+ 13%
Global Y	+ 12%	+ 9%
Global Z	+ 17%	+ 13%
Ligament		
Anterior longitudinal ligament	- 22%	+ 46%
Posterior longitudinal ligament	- 22%	+ 67%
Capsular ligament	0 %	+ 85%
Ligament flavum	+ 10%	+ 79%
Ligament flavum	+ 48%	- 6%